DESIGN AND MODELING OF A PARALLEL ROBOT FOR ULTRASOUND GUIDED PERCUTANEOUS NEEDLE INTERVENTIONS

A Thesis

by

Sabri Orçun Orhan

Submitted to the
Graduate School of Sciences and Engineering
In Partial Fulfillment of the Requirements for
the Degree of

Master of Science

in the
Department of Mechanical Engineering

Özyeğin University
August 2015

DESIGN AND MODELING OF A PARALLEL ROBOT FOR ULTRASOUND GUIDED PERCUTANEOUS NEEDLE INTERVENTIONS

Approved by:

Assist. Prof. Dr. Özkan Bebek, Advisor
Department of Mechanical Engineering
Özyeğin University

Assoc. Prof. Dr. Kemalettin Erbatur
Faculty of Engineering and Natural Sciences
Sabanci University

Assist. Prof. Dr. Barkan Uğurlu
Department of Mechanical Engineering
Özyeğin University

Date Approved: 3 August 2015

To my loved ones

ABSTRACT

Percutaneous needle operations need precise positioning in order to collect samples for diagnosis. Due to their robustness, accuracy robotic systems started to take place in medical procedures. Research that have been done until today showed that the robotic systems increase the accuracy of the medical interventions. This thesis presents the design and modeling of a 5DOF parallel robot that is used to conduct biopsies on human bodies, mostly focusing on the abdominal region. Ozyegin Biopsy Robot (OBR) consists of 3 stages; front stage, back stage and syringe mechanism. Front stage has 2-DOF and was designed to orient the needle and it serves as a guidance during needle insertion. Back stage has 3-DOF and duty of the back stage is to control the orientation of the needle and to perform the needle insertion. Syringe mechanism was designed to collect samples from body after the needle insertion. Necessary workspace and torque analyses were conducted in order to design the robot. Kinematic calculations were performed to find accurate needle tip position. Dynamic equations of motion were derived and system identification was performed on the robot to find the dynamics of system. With the calibration procedures, needle tip accuracy was aimed to be increased. For creating robust and accurate controllers, gravity compensation and friction modeling were implemented on the robot. Three different controller were created; PID controller, pole placement controller and torque computed controller. Results showed that torque computed controller reaches submilimeter needle tip accuracy and was verified as a robust controller for the system.

ÖZETÇE

Deri altına uygulanan iğneli müdahaleler teşhis için kesin pozisyonlamaya ihtiyaç duymaktadır. Gürbüzlükleri ve doğrulukları sayesinde robotik sistemler medical uygulamalarda yer edinmeye başlamıştır. Yapılan araştırmalar robotik sistemlerin medikal müdahalelerin doğruluğunu arttırdığını göstermektedir. Bu tez de insanlar üzerinde biyopsi yapabilecek 5 serbestlik dereceli bir robotun tasarımını ve modellenmesini içermektedir. Özyeğin Biyopsi Robotu (ÖBR) 3 ana bölümden oluşmaktadır; ön taraf, arka taraf ve iğne mekanizması. Ön taraf 2 serbestlik derecesine sahiptir. Ön taraf iğnenin yönünü kontrol etmek ve iğne sokumu sırasında iğneyi yönlendirmek için dizayn edilmiştir. Arka taraf 3 serbestlik derecesine sahip olup iğne yönünü kontrol etmek ve iğneyi vücuda sokabilmek için tasarlanmıştır. İğne mekanizması da iğne sokumu sonrasında numune alımı için oluşturulmuştur. Tasarım esnasında robotun insan üzerinde biyopsu yapabilmesi için yeterli çalışma alanı ve tork analizleri yapılmıştır. Doğru iğne ucu pozisyonunun bulunması için kinematik hesaplamalar uygulanmıştır. Sistem dinamiklerinin anlaşılması için dinamik hareket denklemleri hesaplanmış aynı zamanda robot üzerinde sistem tanımlaması gerçekleştirilmiştir. Kalibrasyon yöntemleri ile iğne ucu pozisyonunun doğruluğunun arttırılması hedeflenmiştir. Gürbüz denetleyici yaratabilmek için robot üzerinde yerçekimi dengelemesi ve sürtünme modellemesi uygulanmıştır. Robot üzerinde denenmek üzere üç farklı denetleyici tasarlanmıştır; Oransal-Türevsel-İntegral denetleyici, kutup yerleştirmeli denetleyici ve hesaplamalı tork denetleyici. Sonuçlar hesaplamalı tork denetleyicinin milimetrenin altında iğne ucu doğruluğuna ulaşabildiğini göstermiş ve denetleyicinin sistem için gürbüz bir denetleyici olduğunu ispatlamıştır.

ACKNOWLEDGEMENTS

First of all, I would like to sincerely thanks to Dr. Özkan Bebek, my thesis advisor, for his guidance and patience throughout this work. I would also like to thank Dr. Barkan Uğurlu for his guidance and informative comments. Special thanks to Ulaş Yıldırım, Mehmet Can Yıldırım, Görkem Muttalip şimşek and Candemir Döğer for their effort,support and inspiration during this work which I thought without them I would not be able to succeed.

Most of all, I would like to dedicate this work to my family who support me with their immeasurable love throughout my studies.

This research was done in the Robotics Laboratory at Ozyegin University; supported by the Scientific and Technical Research Council of Turkey (TUBITAK) under Grant No. 112E312.

TABLE OF CONTENTS

LIST OF TABLES

LIST OF FIGURES

CHAPTER I

INTRODUCTION

Percutaneous needle operations, such as biopsy, are performed to collect samples from critical sample locations such as tumors, organs and glands to observe the existence, extent and origin of a disease. Collected samples are important for the diagnostics, hence the samples must be collected from the exact place of the tumor or the anomaly for further analysis. Nowadays, percutaneous needle operations are performed by hand under the surveillance of a doctor with or without image guidance. Without image guidance, place of the anomaly is sensed by hand by the doctor and operation is performed according to sense of the doctor without any image feedback inside the body. As finding the location of the anomaly depends on the human sense, these operations are only conducted where the anomaly is near skin region. For image guidance during percutaneous needle operations; Magnetic Resonance (MR), Computed Tomography (CT) or Ultrasound (US) are widely preferred system. Target position is detected from medical images and needle is inserted by hand to reach the target position. During insertion, medical images give feedback to the doctor about where the needle tip is inside the body and it is used to reach the position of anomaly accurately. The challenge of the operation is to take enough samples with least number of trials to prevent damage to the healthy tissue. As the complexity of the task increases, need for more robust and high precision systems to fulfill the task also increases. Accuracy, robustness and precision of robotic systems provide a new research area under percutaneous needle operations. Using robotic systems, full-autonomous or half-autonomous system were designed and proved high precision and accuracy during percutaneous needle operations.

This thesis presents design and modeling of a 5-DOF robotic system that is capable of conducting biopsies on human bodies. The robot presented here was named as Ozyegin Biopsy Robot(OBR). The aim of the thesis is to develop a full-autonomous robotic system that is able to insert the needle to the body and to reach a target position inside the body. System is designed for multi-purpose biopsy procedures, mostly focusing on the abdominal region. With a given target position where the anomaly is detected, robot can position itself with a desired attitude. Needle insertion is performed by the robot autonomously. With minor changes at the end-effector, drug delivery procedures could also be applied.

Ozyegin Biopsy Robot (OBR) that is represented in this thesis will be the base of a 2D ultrasound image guided robotic system which will conduct biopsies on humans (Figure 1). General idea is to find target tissue inside body using ultrasound images and guide the robot through the target position. In order to do that a robotic arm will position the ultrasound probe on the human body. Images from the ultrasound will be evaluated and the target tissue position will be located. The robot will position itself to insert the needle to reach the target position. During the insertion, the needle will be tracked through the ultrasound images and the needle tip position will be feedback to the robot in order to increase target reach accuracy. The purpose is to conduct biopsies fully autonomous.

Ozyegin Biopsy Robot (OBR) is a 60% scaled up version of Small Animal Biopsy Robot (SABiR) with necessary improvements to gain capability of performing biopsies on humans [1]. Design structure of the two robot show similarities as both robots have 5-DOF. The main difference between the robots are their aim of use. SABiR was designed to conduct biopsies on small animals. On the other hand, OBR was designed to conduct biopsies on human bodies.

Contribution of this thesis is the design of a robot that can conduct biopsies on human bodies, especially on the abdominal region. Workspace analysis were performed

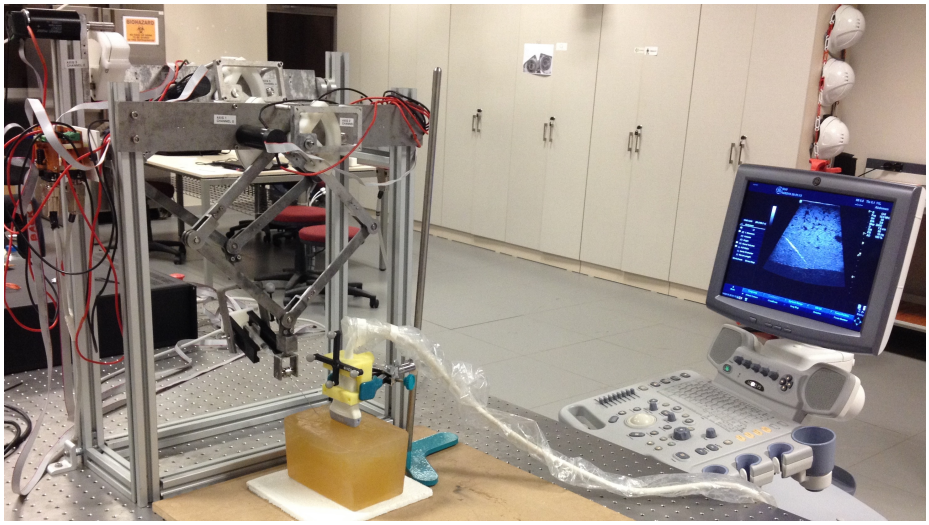

Figure 1: System consists of the Ozyegin Biopsy Robot (OBR) and an Ultrasound machine

during design process for the robot to have at least workspace of 50 cm cube that will cover the abdominal region. For the back stage gravity compensation, rhombus structure of the back stage was simplified into one bar mechanism. Simplified mechanism generates more robust results and the robot were able to hold its position while canceling gravity effects on the robot. Friction on each joint were inspected with a disturbance observer. Friction models for each joint were created using disturbance observer data and tested on each joint. Therefore, friction models of the system were improved into a more robust model. Torque computed controller was implemented on the robot. The reason of choosing a torque computed controller was to decrease the effort of controller on the system and to reach submilimeter accuracy. Results showed that torque computed controller reached submilimeter needle tip accuracy and it is verified as a robust controller for the system.

This thesis consists of seven chapters. Chapter I presents problem statement and the solution that is provided to the necessity of high precision systems during percutaneous needle operations. Chapter II discusses the research that have been done on robotic assisted percutaneous needle interventions. Design procedures and design of the robot is provided in Chapter III. Chapter IV explains the kinematics

and dynamics of Ozyegin Biopsy Robot. Calibration procedures and modeling of the robot is discussed on Chapter V. Chapter VI describes the control architectures implemented on the robot and presents the results of controllers. Finally, Chapter VII concludes the thesis by summarizing the work done and comparing the results.

CHAPTER II

BACKGROUND

For surgical tasks, robots are developed using two control methods; teleoperation and autonomous operations. These systems use Magnetic Resonance (MR), Computed Tomography (CT), or Ultrasound (US) imaging for the target positioning. For teleoperation, robots are controlled by doctors during medical procedures. On the other hand, for autonomous systems, robots function by itself under the surveillance of doctors. Main purpose of these systems is to increase accuracy and reliability of the needle operations. As these systems were designed to conduct medical operations on different body parts and organisms such as lung [2]-[3], kidney [4], breast [5]-[6]-[7]-[8], brain [9]-[10]-[11] and small animals [12]-[13]-[14]-[1]-[15]; they had different design requirements and have custom designs to meet the requirements of specific tasks.

Among these custom developed medical robotic systems, a needle insertion device which has 4 degree of freedom (DOF) with five chains systems was developed by Chung et al. [12]. System has a singularity-free design. Goffin et al. [13] developed another system for needle operations on small animals, with 6 DOF. Mechanism consist μCT and stereo camera systems for the positioning, after μCT imaging, biopsy is performed on the stabilized animal with using stereo camera guidance. After this two staged imaging system, they achieve 0.17 $\pm$ 0.091mm in x direction and 0.13 $\pm$ 0.093mm in z direction mean positioning error. Another small animal biopsy robot is developed by Huang et al. [14] different than Goffin et al. The design of the robot is compatible with MRI. Robot was developed with mounting syringe fixture to CAST-PRO II robot arm (SONY Electronics Inc.), robot has reached to 0.05 $\pm$ 0.39

mm positioning accuracy. Another custom made robot with 5-DOF was designed by Bebek et al. [1] to conduct biopsy on small animals. System has a bandwidth of 4 Hz and reached needle tip accuracy of 0.4 mm RMS. Waspe et al. [15] developed a robotic system that will be used small animal biopy procedures with image-guidance. Robot has 3-DOF, 2-DOF for needle orientation(pitch and roll) and 1-DOF for needle insertion. Experiments proved that the system reached positioning accuracy of 54 $\pm$ 12μm and 91 $\pm$ 21μm in pitch and roll axes, respectively.

Yang et al. [6] developed a breast biopsy robot which is actuated pneumatically and use MRI imaging. Robot is parallel mechanism with 4 DOF. Tanaiutchawoot et al. [5] designed a passive robotic needle holder based on breast features for breast biopsy. System has 5 DOF and uses real time optical tracking system for positioning. Another breast biopsy mechanism was designed by Nelson et al.[7]. A 6-DOF articulated arm was integrated into system to reach desired position and to conduct biopsy. Finding target location and image guidance are performed by ultrasound volume image data. Moon et al. [2] designed a parallel mechanism to correct possible misalignment caused by the property of the skin the needle insertion for lung biopsy. Also Moon et al. [16] designed another system for a complex situation, in which the needle tip is bended because of the skin's stiffness. This two DOF system prevents the needle slippery.

Zaidi et al. [9] developed an MRI compatible robot to perform needle interventions such as biopsy and brachytherapy for neurosurgery procedures. System consist of 5-DOF; first 3-DOF is a Delta parallel manipulator to control positioning of the robot and last 2-DOF is rotational serial manipulator to control the orientation of the needle. Another MRI compatible image-guided robot for percutaneous needle operations was designed by Melzer et al. [11]. Robot has 5-DOF and it is attached to a 2-DOF bed to manage preorientation. During experiments, robot reached precision in axial side of $\pm$ 1mm and accuracy of angle in transverse plane of $\pm$ 1°. Raoufi et

al. [10] designed a tele-operated robotic system for neurosurgery operations. Robotic system is MRI compatible and consists of 3 stages; surgical arm, navigation module, biopsy module. Surgical arm controls position, navigation module controls orientation and biopsy module controls needle insertion. In total, system has 10-DOF. Zhou et al. [3] developed an experimental system for biopsy of lung nodules. System is operated with a 6-DOF robot manipulator. Aim of the system is to cancel out the effect of respiratory motion.

Ozyegin Biopsy Robot (OBR) that is presented in this thesis has 5-DOF. The robot is designed to conduct biopsies on human bodies, especially on the abdominal region. Due to necessity of precise positioning during percutaneous needle operations, submilimeter needle tip accuracy was aimed for the design of the robot. OBR is the base of a 2D ultrasound image guided robotic system. Using ultrasound images, target position will be detected and the robot will position itself to insert needle. During insertion, needle tip will be tracked through ultrasound images and positional information will be fed to the robot to increase needle tip accuracy. Purpose of this robotic system is to conduct biopsies on human bodies fully autonomous. As the system will be fully autonomous, respiratory motion would decrease the needle tip accuracy. Due to the design, dynamic capability of the robot would provide necessary movement to cancel out the effects of respiratory motion.

CHAPTER III

DESIGN OF THE ROBOT

A robotic system needs at least 6-DOF to reach any point in 3-D space in any orientation. The aim of the Ozyegin Biopsy Robot (OBR) was to insert needle to body in order to conduct biopsy. Rotation around the needle axis was redundant for the design, hence, OBR was decided to have 5-DOF in order to perform needle insertion operations. The robot was divided into two parts, front stage and back stage (Figure 10). Two stages were designed to be parallel to each other and would carry the needle. A rhombus mechanism was decided to control the end-effectors of stages. The reason of choosing a rhombus mechanism was to simplify kinematic calculations. Each rhombus mechanism would be controlled by 2 DC motors, hence each stage has 2-DOF in order to control end-effector position. These 4-DOF would satisfy to reach desired needle orientation. A third DOF was added to back stage to provide the robot needle insertion capability. Every stage was designed to have a gimbal mechanism which has 2-DOF at their end-effectors. Gimbals were designed to provide needle and syringe mechanism free rotation around the end-effectors of stages. Their DOF are passive for the system. Therefore, OBR was designed to have 5 active DOF, 4-DOF (2 active and 2 passive) on front stage and 5-DOF (3 active and 2 passive) on back stage. Appearance of whole robot can be seen in Figure 10.

After designing general shape of the robot, first step was the workspace analysis in order to find link lengths of rhombus mechanism. Workspace of the robot covers the volume where the needle tip can reach in 3D space. Design criteria of the workspace is that the body part where the biopsy will be performed should be in the workspace of the robot. As Ozyegin Biopsy Robot was designed to conduct biopsy on

abdominal region, workspace of the robot is decided to cover at least a cube of 50 cm. Calculations were conducted as each-DOF is moved by 1 degree to find a new needle tip position. Positions were mapped on a graph to generate the volume of workspace. Calculations were conducted for different link lengths. Length of the biopsy needles in the market ranges from 9 cm to 20 cm. Therefore, distance between the front stage and the back stage is kept constant at 250 mm during calculations to come up with a design that is suitable with every size of the biopsy needle. The workspace analysis for 200 mm link length can be seen in Figure 2. When the simulation results were compared, minimum link length that would satisfy the design criteria was found as 200 mm. Design of OBR was carried on according to the 200 mm link length.

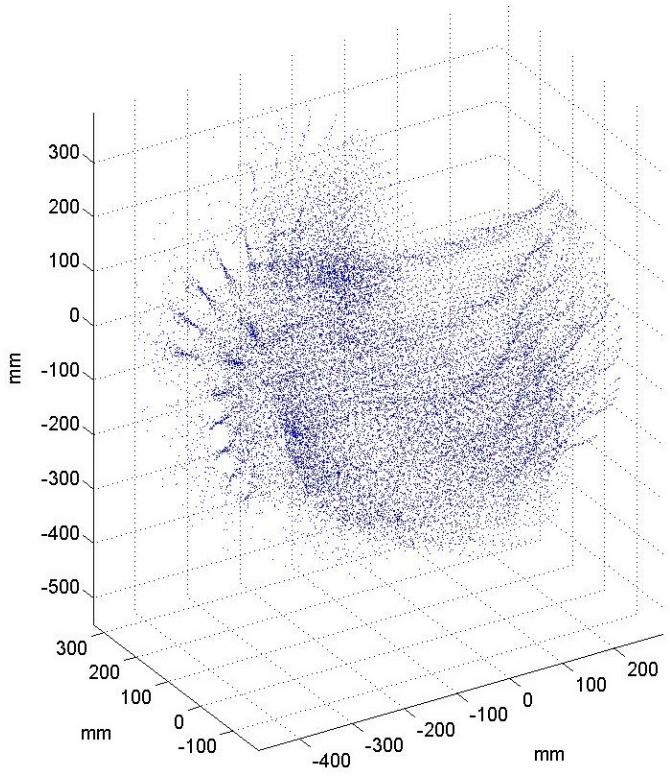

Figure 2: Workspace analysis of OBR with 200mm link lengths

After specifying the link lengths, the robot was designed. During the design process, one of the problem encountered was the moment that occurred due to long

links. According to FEM analysis, the links were bending as the force is applied from tissue to the links through the needle. FEM analysis showed that increasing link thickness from 3 mm to 4 mm decreased the bending deflection by 50%. Figure 3 shows the comparison of the different links thicknesses. 1 N force was applied to the free end of the links and deflections were observed at the analysis. Disadvantage of increasing the thickness of links was increasing total weight and inertia of moving parts, because links are the moving parts of the robot. One of the goal of the design was to keep inertia of the system in a minimum level. Therefore, thickness of links was chosen as 4 mm.

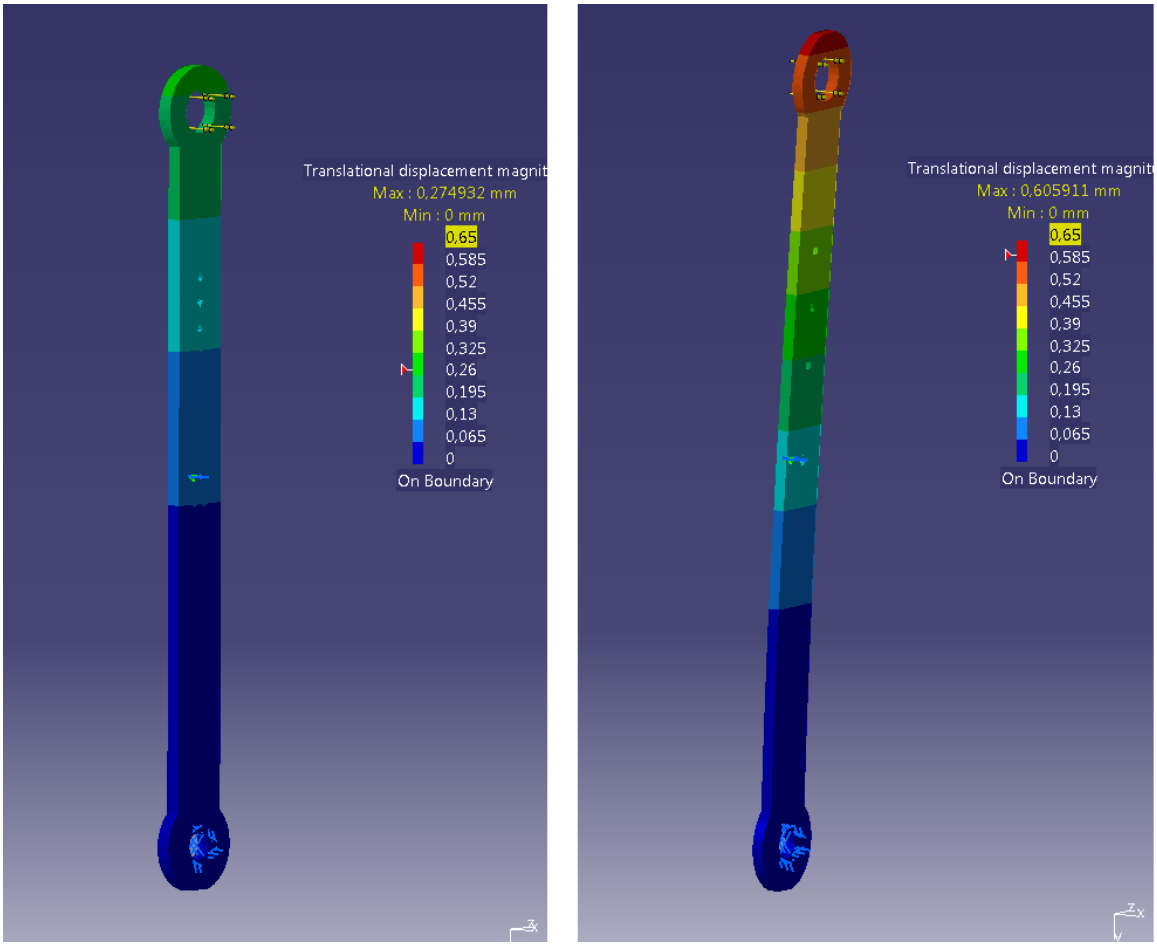

Figure 3: FEM analysis for different link thickness. Results showed that with 3 mm thickness maximum displacement is 0.60 mm, with 4 mm thickness maximum displacement is 0.27 mm. Bending deflection is reduced by 50%

After finishing the first prototype design of robot, torque analysis was performed on the robot to in order to select actuators for the robot. To find that a circular path where the end-effector moves at 5 Hz is generated and a simulation was conducted. The necessary torque values to perform the trajectory tracking were calculated using the dynamic equations of OBR. Figure 4 shows the results of the torque analysis for the front stage. As seen in Figure 4 the maximum torque that should be provided by the motors is around 250 mNm. In the design, a disc to capstan ratio of 10.8 is used to transfer the torque from the motor shaft to the link, hence necessary actuator torque value for motors was calculated as 20 mNm. As the simulation is conducted for a single frequency, to cover different velocity, frequency profiles and to count for friction on the system; safety factor of 4 was applied to choose the appropriate motor. To fulfill the motion generation, Maxon RE30 DC motors which have nominal torque of 85.6 mNm were chosen. Simulation for the back stage was conducted using the path created for front stage. During simulation Axis3 is kept constant at 0°. Necessary torque values for Axis4 and Axis5 are shown in Figure 5. Simulation suggested that maximum torque value will be 400 mNm. Same disc to capstan ratio of 10.8 is used for Axis4 and Axis5 in the design, hence, necessary actuator torque value to fulfill the motion was calculated as 40 mNm. To count for different velocity profiles and friction on the system, safety factor of 4 was applied for motor selection. Maxon RE40 DC motor was chosen for Axis4 and Axis5 with a nominal torque of 170 mNm. For the third axis in the back stage a different simulation was conducted. In the simulation Axis4 and Axis5 were kept constant at 260° and 280°, respectively. The reason for this choice was that rhombus structure would be on the longest position, hence to move the structure Axis3 would need higher torque values. Axis3 was moved from -50° to 50° at 5Hz during simulation. Results are shown at Figure 6. Maximum necessary torque value was 500 mNm. Disc to capstan ratio was design as 12.5 for Axis3, hence necessary actuator torque value was calculated as 40 mNm. Safety factor of 4 was

applied to count for different velocity profiles and friction on the system. Maxon RE40 DC motor was chosen for Axis3 with a nominal torque of 170 mNm.

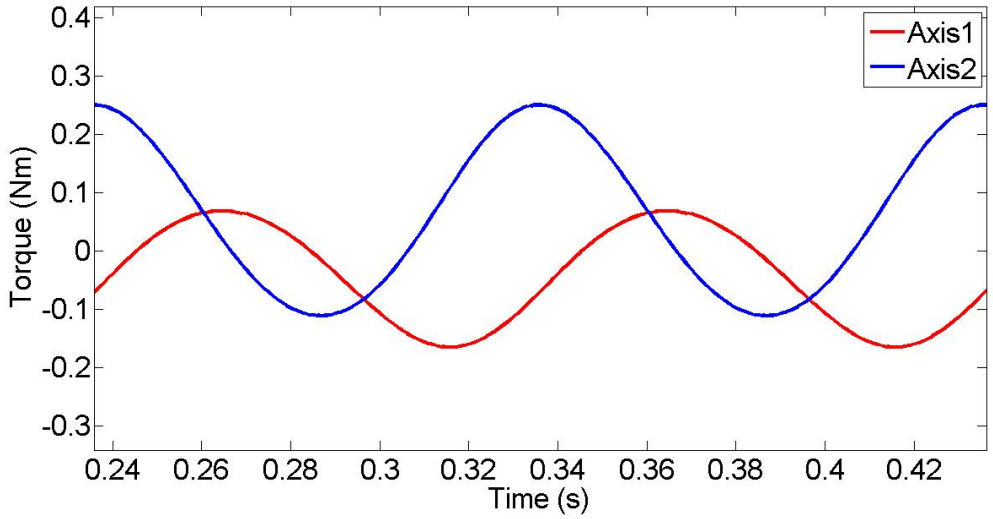

Figure 4: Torque analysis for front stage to choose actuators

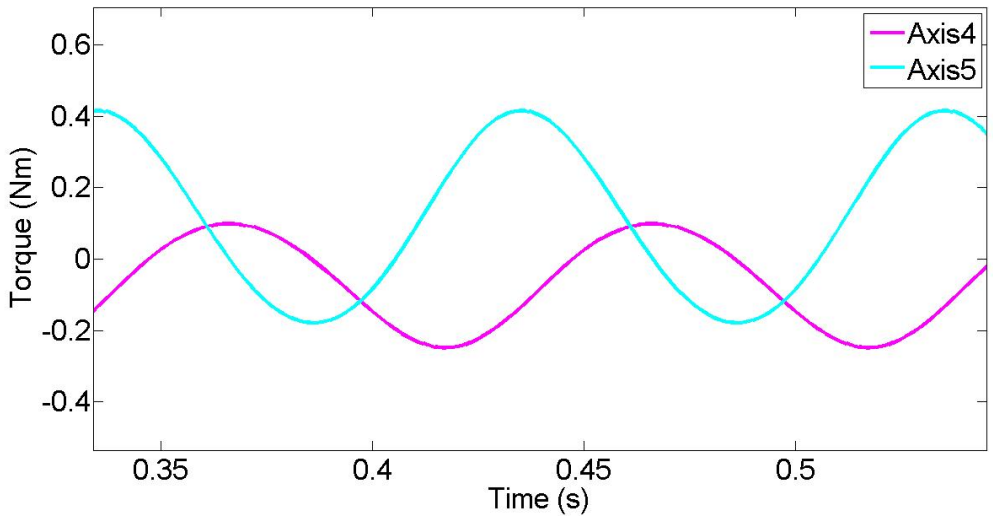

Figure 5: Torque analysis for Axis4 and Axis5 in back stage to choose actuators

Design of OBR consists of 5-DOF and 3 main stages; front stage, back stage, syringe mechanism (Figure 10). Main purpose of the front stage is to give guidance to the needle during insertion. Needle insertion is carried out by the back stage. Syringe mechanism was designed to get sample from body or to deliver drug to a specified part

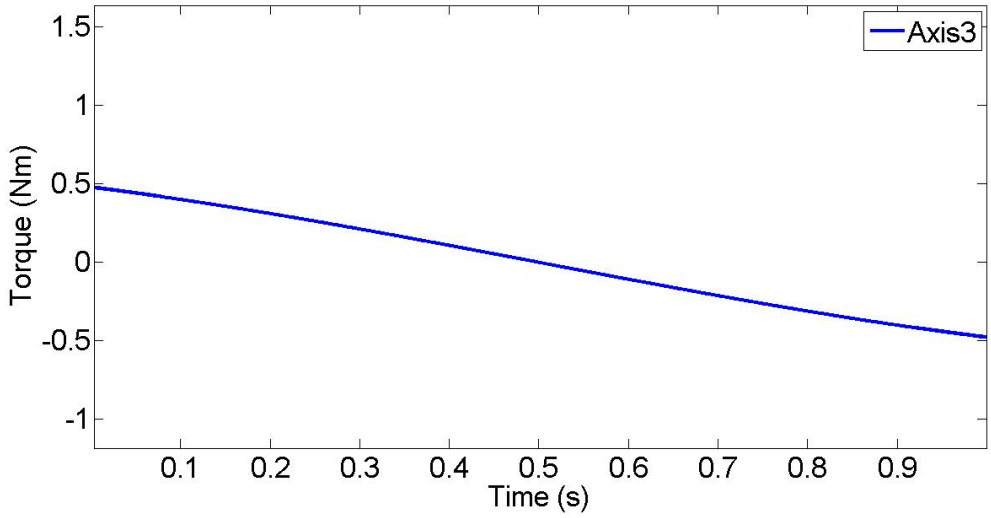

Figure 6: Torque analysis for Axis3 in back stage to choose actuators

of the body. Actuation of 5DOF is conducted by tendon-driven mechanisms. Tendon-driven mechanism consists of a quarter disc connected to link, a shaft connected to the motors and 7×7 stainless steel tendons. Two ends of tendon are attached to the disc through vented-screws which are used to adjust the tension on the tendon. From one end, tendon goes through the circular portion of the disc and makes 3coils around the shaft. After those coils, the loose end of the tendon is attached to the screw. Advantage of using tendon-driven mechanism is to remotely control of moving parts. In a rhombus structure, actuation of moving links are carried out by motors that are connected to stationary base, hence inertia of the moving parts are reduced. In addition, tendon-driven mechanisms have no backlash when compared to geared systems.

3.1 Front Stage

Main elements of the stage consist of one stationary base and four moving links that can be seen in Figure 7. Four links are arranged to form a rhombus. Two links are connected to two discs which are actuated by tendon-driven mechanisms. With the help of a shaft passes through the center of discs, discs are attached to the stationary

base. Discs could easily rotate around the shaft. Links are assembled to each other with L-shape extensions which are designed to prevent backlash on the system. As the discs are attached to the stationary base, one edge of the rhombus is fixed to the stationary base. The edge opposite to the fixed edge is free to translate. 2 DC motors are attached to the stationary base in order to actuate tendon-driven mechanism to control the position of end effector. As the motors are connected to the stationary base and remotely control the end effector position, inertia of the moving parts is reduced. A gimbal mechanism with 2DOF is connected to the end effector of the 5-bar linkage with a 45° reference angle to simplify the kinematic calculations of the rhombus. The purpose of the gimbal is to guide the needle during insertion. The needle passes through the gimbal and rotates freely around the rotational axes of the gimbal. No torsional effect is applied to the needle by the gimbal.

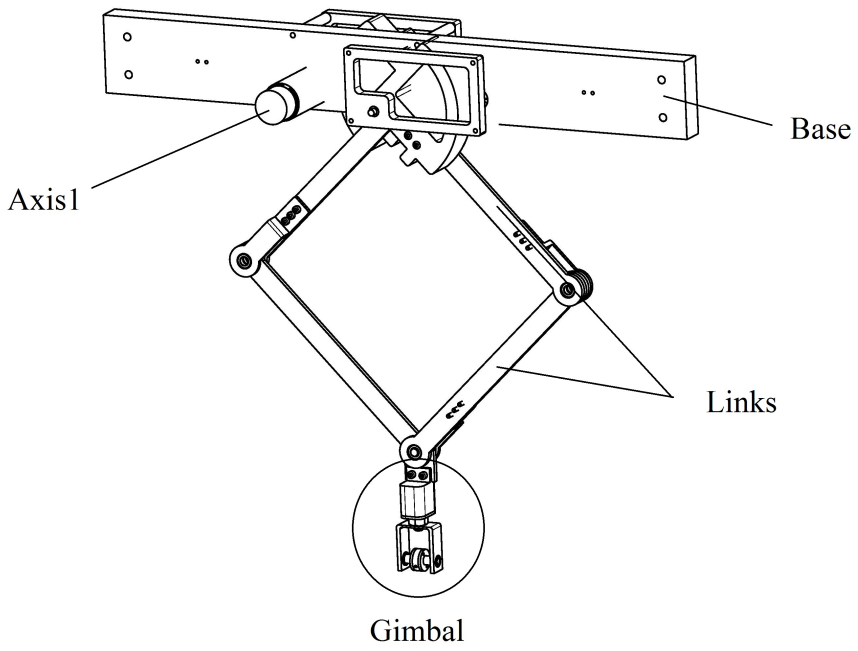

Figure 7: View of front stage

3.2 Back Stage

Design of the back stage and front stage are quite similar with an addition of a rotational axis. Figure 8 shows the design of back stage. Back stage also consists of a base and four links. The links are arranged to form a rhombus. Two discs are connected to two links in order to provide actuation to the rhombus structure. One edge of rhombus is fixed to the base through the shaft that is passing from the center of discs. Motion of the free edge is provided by tendon-driven mechanism that is controlled by 2 DC motors. Main difference between the back stage and the front stage is that the base in the back stage also rotates around third axis which is controlled by a DC motor. Rotation around third axis pushes back stage towards the front stage. This motion provides robot ability to insert a needle to the target position through the gimbal of the front stage. Another gimbal mechanism with 2DOF is connected to the end effector of the 5-bar linkage in the back stage. Gimbal mechanism is also assembled to the end effector of back stage with a 45° reference angle. This gimbal carries the syringe mechanism which can freely rotate around the rotational axes of the gimbal.

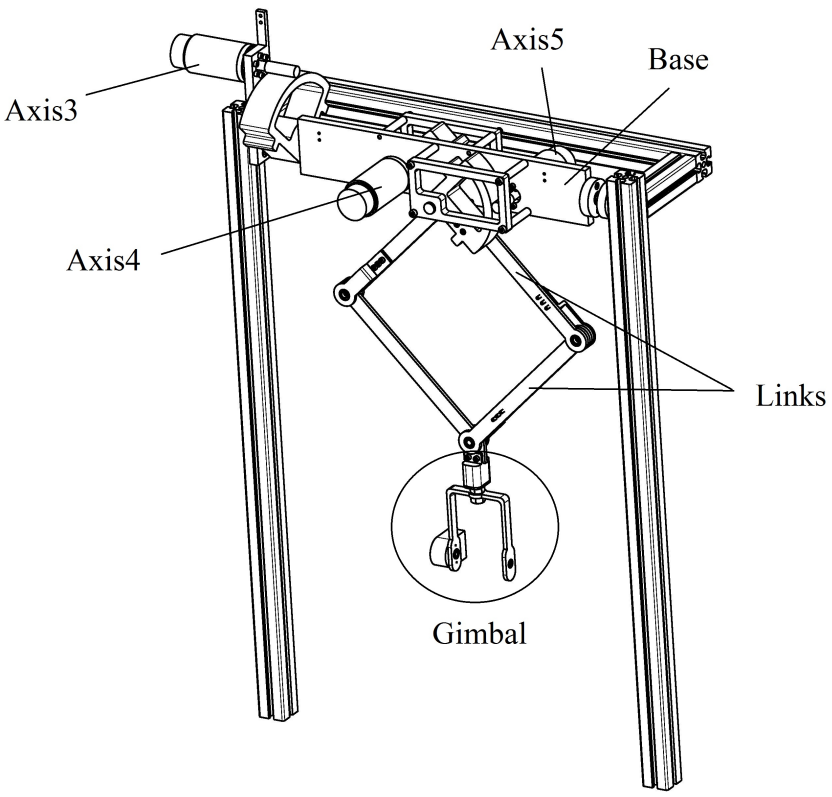

Figure 8: View of back stage

3.3 Syringe Mechanism

The syringe mechanism is designed to get samples from target position inside the body (Figure 9). Mechanism is the connection part between the front stage and the back stage. It is mainly carried by the back stage which effects the inertial behavior of the back stage. The needle connected to the syringe mechanism passes through the gimbal in the front stage. Getting sample process from body starts with the needle insertion by the back stage. After needle tip reaches the target position inside the body, sample is collected with the help of motor on the syringe mechanism. Motor torque is transferred through a lead screw into linear translation. This motion controls the part inside the needle to collect samples. Despite the syringe mechanism was designed to get samples from body, in the experiments to control the robot only 22 gauge biopsy needles were used without sample collection.

In the design of syringe mechanism, an Avago HEDR-55L2-BY07 high resolution encoder was attached to the gimbal of back stage to measure the offset between the needle and syringe mechanism. In theory, the needle is mounted to the syringe mechanism at the back stage without any angular offset. However, during the assembly process, needle is not mounted perfectly aligned to the syringe mechanism. In order to calculate needle tip position correctly, offset of needle should be measured and be integrated inside kinematic calculations. Details of needle offset integrated kinematic calculations will be given in Chapter IV.

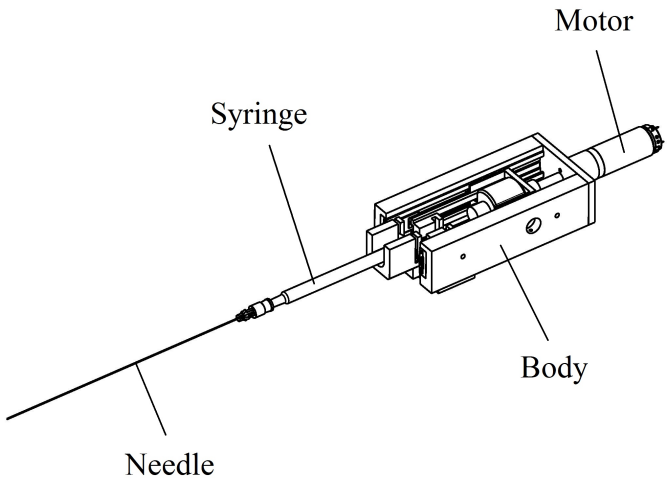

Figure 9: View of syringe mechanism

All parts of the robot were manufactured at Ozyegin University Manufacturing and Technologies Laboratory using CNC Lathe and CNC Milling machines. In order to create a lightweight robot, parts of OBR except discs were manufactured from 6063

aluminium alloy. Discs of the design were manufactured from synthetic polymer, Delrin. The reason of using Delrin for discs is that as the discs are part of tendon-driven system, Delrin shows low friction and high stiffness characteristics. First prototype of the robot was assembled to analyze any failures in the design. One major problem of the first prototype was the backlash at the link joints due to applied external forces. When the force was applied, the links were rotated around an axis perpendicular to joint axis. Joint design of the robot was insufficient to prevent the backlash. As a solution, the shaft was screwed to the link. This design prevents the link to rotate around any other axis except from the joint axis and solves the stiffness problem of the robot. Another problem was in the design of the front stage. The front stage had a design where the motors were facing to the same direction. In the robot design, as mentioned before, tendon-driven system consists of one disc connected to link and one shaft connected to motor. Due to the design of front stage, one of the shafts in tendon-driven system had twice the length of other shaft. The tension on the steel wire was creating moment on the motor shaft. To prevent any potential damage to motor, design of front stage was changed. A replica of the back stage design was applied to the front stage.

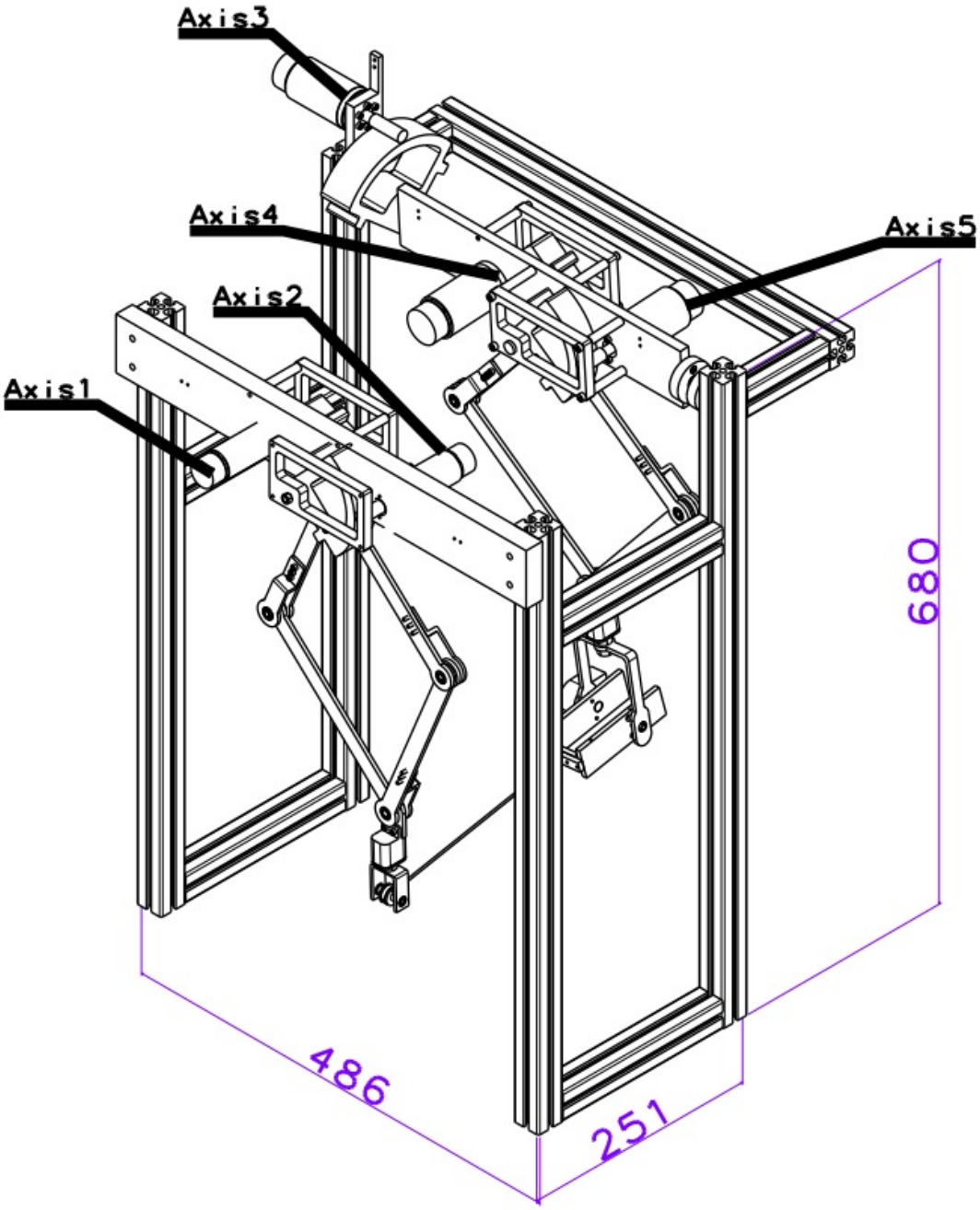

Figure 10: Ozyegin Biopsy Robot (OBR)

CHAPTER IV

KINEMATICS AND DYNAMICS OF OZYEGIN BIOPSY ROBOT

4.1 Kinematics of OBR

4.1.1 Forward Kinematics

In order to find accurate needle tip position forward kinematics of the robot was derived. As mentioned before, OBR has 3 main stages; front stage, back stage and syringe mechanism. Orientation of the syringe mechanism depends on the positions of the end-effectors of the front stage and the back stage. To find the positions of the end-effectors, forward kinematics of the two stages were solved. Coordinate frame orientations and joint numbers are shown in Figure 11. $\{F\}$ and $\{B\}$ represent the front stage coordinate system and the back stage coordinate systems respectively. l_f is the front stage link length, l_b is the back stage link length, l_{fg} is the distance between last joint of the front stage and the front stage gimbal, l_{bg} is the distance between last joint of the back stage and the back stage gimbal. In order to find the forward kinematics, Denavit-Hartenberg convention was applied to OBR. Denavit-Hartenberg parameters can be seen in Tables 1 and 2.

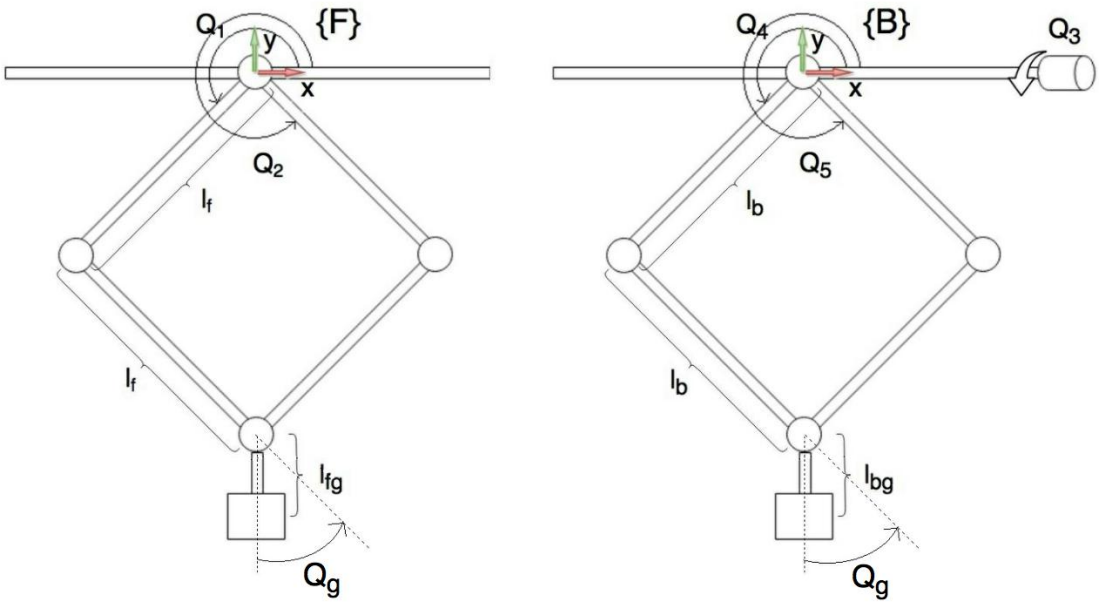

Figure 11: Coordinate frames and joint orientations for front stage and back stage

	a_{i-1}	α_{i-1}	d_i	θ_i
1	0	0	0	θ_1
2	l_f	0	0	$\theta_2 - \theta_1$
3	l_f	0	0	-θ_g
E	l_{fg}	0	d_{fg}	0

Table 1: Denavit-Hartenberg parameters for front stage

	a_{i-1}	α_{i-1}	d_i	θ_i
1	0	0	0	90
2	0	90	0	0
3	0	0	0	θ_3
4	0	-90	0	$\theta_4 - 90$
5	l_b	0	0	$\theta_5 - \theta_4$
6	l_b	0	0	-θ_g
E	l_{bg}	0	d_{bg}	0

Table 2: Denavit-Hartenberg parameters for back stage

Transformation matrices between joints from base of front stage to the end-effector

of front stage can be written from Denavit-Hartenberg parameters as

$$\mathrm{T}_1^B = \begin{bmatrix} \cos(\theta_1) & -\sin(\theta_1) & 0 & \mathrm{l}_f \\ \sin(\theta_1) & \cos(\theta_1) & 0 & 0 \\ 0 & 0 & 1 & 0 \\ 0 & 0 & 0 & 1 \end{bmatrix} \tag{1}$$

$$\mathrm{T}_2^1 = \begin{bmatrix} \cos(\theta_2 - \theta_1) & -\sin(\theta_2 - \theta_1) & 0 & \mathrm{l}_f \\ \sin(\theta_2 - \theta_1) & \cos(\theta_2 - \theta_1) & 0 & 0 \\ 0 & 0 & 1 & 0 \\ 0 & 0 & 0 & 1 \end{bmatrix} \tag{2}$$

$$\mathrm{T}_3^2 = \begin{bmatrix} \cos(-\theta_g) & -\sin(-\theta_g) & 0 & \mathrm{l}_f \\ \sin(-\theta_g) & \cos(-\theta_g) & 0 & 0 \\ 0 & 0 & 1 & 0 \\ 0 & 0 & 0 & 1 \end{bmatrix} \tag{3}$$

$$\mathrm{T}_E^3 = \begin{bmatrix} 1 & 0 & 0 & \mathrm{l}_{fg} \\ 0 & 1 & 0 & 0 \\ 0 & 0 & 1 & \mathrm{d}_{fg} \\ 0 & 0 & 0 & 1 \end{bmatrix} \tag{4}$$

Back stage transformation matrices can be found as

$$\mathrm{T}_1^B = \begin{bmatrix} 0 & -1 & 0 & 0 \\ 1 & 0 & 0 & 0 \\ 0 & 0 & 1 & 0 \\ 0 & 0 & 0 & 1 \end{bmatrix} \tag{5}$$

$$\mathrm{T}_2^1 = \begin{bmatrix} 1 & 0 & 0 & 0 \\ 0 & 0 & -1 & 0 \\ 0 & 1 & 0 & 0 \\ 0 & 0 & 0 & 1 \end{bmatrix} \tag{6}$$

$$\mathrm{T}_3^2 = \begin{bmatrix} \cos(\theta_3) & -\sin(\theta_3) & 0 & 0 \\ \sin(\theta_3) & \cos(\theta_3) & 0 & 0 \\ 0 & 0 & 1 & 0 \\ 0 & 0 & 0 & 1 \end{bmatrix} \tag{7}$$

$$\mathrm{T}_4^3 = \begin{bmatrix} \cos(\theta_4 - 90) & -\sin(\theta_4 - 90) & 0 & 0 \\ 0 & 0 & 1 & 0 \\ -\sin(\theta_4 - 90) & -\cos(\theta_4 - 90) & 0 & 0 \\ 0 & 0 & 0 & 1 \end{bmatrix} \tag{8}$$

$$\mathrm{T}_5^4 = \begin{bmatrix} \cos(\theta_5 - \theta_4) & -\sin(\theta_5 - \theta_4) & 0 & \mathrm{l}_b \\ \sin(\theta_5 - \theta_4) & \cos(\theta_5 - \theta_4) & 0 & 0 \\ 0 & 0 & 1 & 0 \\ 0 & 0 & 0 & 1 \end{bmatrix} \tag{9}$$

$$\mathrm{T}_6^5 = \begin{bmatrix} \cos(-\theta_g) & -\sin(-\theta_g) & 0 & \mathrm{l}_b \\ \sin(-\theta_g) & \cos(-\theta_g) & 0 & 0 \\ 0 & 0 & 1 & 0 \\ 0 & 0 & 0 & 1 \end{bmatrix} \tag{10}$$

$$\mathrm{T}_E^6 = \begin{bmatrix} 1 & 0 & 0 & \mathrm{l}_{bg} \\ 0 & 1 & 0 & 0 \\ 0 & 0 & 1 & \mathrm{d}_{bg} \\ 0 & 0 & 0 & 1 \end{bmatrix} \tag{11}$$

When the transformation matrix between base and end-effector is calculated, the position of end-effectors according to the base of stages can be found as

$$\mathrm{p}_f = \begin{bmatrix} \mathrm{l}_f cos(\theta_1) + l_f cos(\theta_2) + l_{fg} cos(\theta_2 - \theta_g) \\ \mathrm{l}_f sin(\theta_1) + l_f sin(\theta_2) + l_{fg} sin(\theta_2 - \theta_g) \\ \mathrm{d}_{fg} \end{bmatrix} \tag{12}$$

$$\mathrm{p}_b = \begin{bmatrix} \mathrm{l}_b cos(\theta_4) + l_b cos(\theta_5) + l_{bg} cos(\theta_5 - \theta_g) \\ \text{- } \mathrm{d}_{bg} sin(\theta_3) + (l_b sin(\theta_4) + l_b sin(\theta_5) + l_{bg} sin(\theta_5 - \theta_g)) cos(\theta_3) \\ \mathrm{d}_{bg} cos(\theta_3) + (l_b sin(\theta_4) + l_b sin(\theta_5) + l_{bg} sin(\theta_5 - \theta_g)) sin(\theta_3) \end{bmatrix} \tag{13}$$

p_f is the front stage end-effector position according to front stage base coordinate system, p_b is the back stage end-effector position according to back stage base coordinate system. To transform front stage coordinate system into back stage coordinate system, a transformation matrix between two stages was generated with kinematic calibration which will be described in Chapter V.

$$\mathrm{T}_F^B = \begin{bmatrix} 0.999 & 0 & -0.0007 & -1.26 \\ 0 & 0.999 & 0.0048 & -51 \\ 0.0007 & 0.0048 & 0.999 & 246 \\ 0 & 0 & 0 & 1 \end{bmatrix} \tag{14}$$

Hence, front stage end-effector position can be transformed into back stage coordinate system as

$$p_f^B = T_F^B \times p_f^F \tag{15}$$

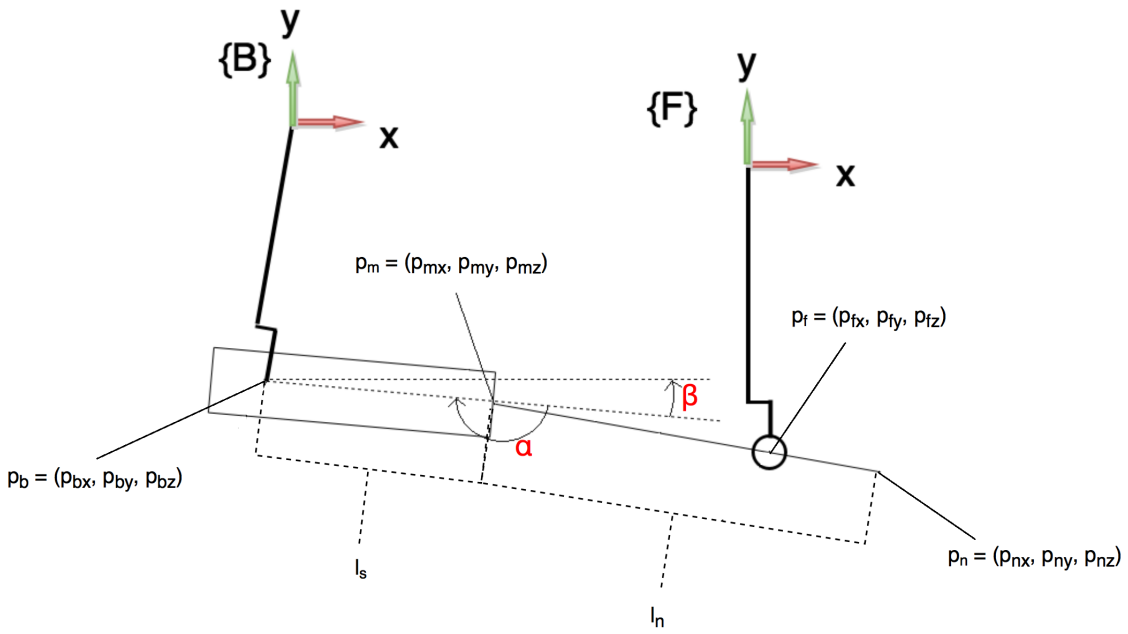

Figure 12: Side view of front stage, back stage, syringe mechanism and needle

In order to find accurate needle tip position, needle mounting offset should be integrated inside forward kinematic calculations. Figure 12 shows the syringe mechanism and needle from a side angle. p_m is the needle mounting position, p_n is needle tip position, β is the syringe mechanism angle, l_s is the length of syringe mechanism and l_n is the length of needle. As β is observed from encoder data at the back stage gimbal, $\vec{r_s}= (\begin{bmatrix} r_{s_i} r_{s_j} r_{s_k} \end{bmatrix})^T$, unit vector along syringe mechanism, could be calculated. l_s is a known parameter from design, hence p_m is calculated as

$$p_m^B = l_s \, \vec{r_s} + p_b^B \tag{16}$$

Indication shows that calculated mounting position is defined in the back stage coordinate system. Next step is to find needle tip position, p_n. In calculations, needle is assumed to be straight and it is known that p_m, p_f and p_n will be on the same line, the needle line. Therefore, needle tip position is calculated using the line equation as

$$\frac{p_{m_x}-p_{f_x}}{p_{m_x}-p_{n_x}} = \frac{p_{m_y}-p_{f_y}}{p_{m_y}-p_{n_y}} = \frac{p_{m_z}-p_{f_z}}{p_{m_z}-p_{n_z}} = \frac{l_d}{l_n} \tag{17}$$

where l_d is the distance between mounting position and front stage end-effector position. Both p_m and p_f are found during kinematic calculations, hence distance between two positions is a known parameter. l_n is also set during design process.

4.1.2 Inverse Kinematics

Forwards kinematics provides the needle tip position with given joint angles. In order to reach a desired needle tip position, inverse kinematics of the robot should also be solved. Desired joint angles that forms the desired needle tip position p_n and orientation $\vec{r_n}$= $(\begin{bmatrix} r_{n_i} r_{n_j} r_{n_k} \end{bmatrix})^T$ are calculated analytically. p_n and $\vec{r_n}$ are provided to the robot and l_n is a known parameter from design. Therefore, p_m is calculated as

$$p_m^B = \mathrm{p}_n^B - l_n \, \vec{r_n} \tag{18}$$

As the needle is assumed to be straight and p_m, p_f and p_n are assumed to be on the same line, line equation is used to find p_f.

$$\frac{p_{m_x}-p_{f_x}}{p_{m_x}-p_{n_x}} = \frac{p_{m_y}-p_{f_y}}{p_{m_y}-p_{n_y}} = \frac{p_{m_z}-p_{f_z}}{p_{m_z}-p_{n_z}} \tag{19}$$

p_f that is found from line equation is in the back stage coordinate system. To calculate desired joint angles to reach front stage end-effector position, transformation from back stage coordinate system to front stage coordinate system is necessary. Transformation matrix, as mentioned before, is determined by kinematic calibration.

$$p_f^F = T_B^F \times p_f^B \tag{20}$$

After finding desired front stage end-effector position according to the front stage coordinate system, desired joint angles to reach that position is calculates from

$$
\begin{gathered}
k_f = \tfrac{l_{fg}}{\sqrt{2}} \ , \ m_f = l_f + k_f \ , \ a_f = 2m_f p_{f_x} - 2k_f p_{f_y} \\
\mathrm{b}_f = 2k_f p_{f_x} + 2m_f p_{f_y} \ , \ c_f = \tfrac{p_{f_x}^2 + p_{f_y}^2 + 2m_f k_f}{\sqrt{a_f^2 + b_f^2}} \\
\theta_2 = atan2(c_f, -\sqrt{1 - c_f^2}) - atan2(a_f, b_f) \\
\mathrm{n}_{1f} = p_{f_x} cos(\theta_2) + p_{f_y} sin(\theta_2) - l_f - k_f \ , \ n_{2f} = -p_{f_x} sin(\theta_2) + p_{f_y} cos(\theta_2) + k_f \\
\theta_1 = atan2(n_{2f}, n_{1f}) + \theta_2
\end{gathered}
\tag{21}
$$

p_m is calculated during inverse kinematics of front stage according to needle tip position and orientation. Needle mounting offset is observed using the encoder data at the back stage gimbal. Offset angle is integrated to find syringe mechanism orientation $\vec{r_s}$. Length of syringe mechanism, l_s, is known, hence back stage end-effector position, p_b, is solved from

$$
p_b^B = \mathrm{p}_m^B - l_s \, \vec{r_s} \tag{22}
$$

After finding position of back stage end-effector, desired joint angles to reach that position is calculated from

$$
\begin{gathered}
\mathrm{y}_{ee} = -\sqrt{p_{b_y}^2 + p_{b_z}^2 - l_{bo}^2}, c_3 = \tfrac{p_{b_y} y_{ee} + p_{b_z} l_{bo}}{p_{b_y}^2 + l_{bo}^2}, s_3 = \tfrac{-p_{b_y} l_{bo} + p_{b_z} y_{ee}}{p_{b_y}^2 + l_{bo}^2} \\
\theta_3 = atan2(s_3, c_3) \\
k_b = \frac{l_{bg}}{\sqrt{2}}, m_b = l_b + k_b, a_b = 2m_b p_{b_x} - 2k_b y_{ee} \\
b_b = 2k_b p_{b_x} + 2m_b y_{ee}, c_b = \frac{p_{b_x}^2 + y_{ee}^2 + 2m_b k_b}{\sqrt{a_b^2 + b_b^2}} \\
\theta_5 = atan2(c_b, -\sqrt{1 - c_b^2}) - atan2(a_b, b_b) \\
n_{1b} = p_{b_x} cos(\theta_5) + y_{ee} sin(\theta_5) - l_b - k_b, n_{2b} = -p_{b_x} sin(\theta_5) + y_{ee} cos(\theta_5) + k_b \\
\theta_4 = atan2(n_{2b}, n_{1b}) + \theta_5
\end{gathered}
\tag{23}
$$

4.2 Dynamics of OBR

Dynamic equations of motion are substantial in order to create accurate controllers. Equations of motion can be written as

$$\mathrm{M}(\theta)\ddot{\theta}+\mathrm{C}(\dot{\theta},\theta)\dot{\theta}+\mathrm{G}(\theta)=\tau \tag{24}$$

where M is inertia matrix, C is Coriolis matrix, G is gravitational effect and τ is joint torque. Lagrangian method was used to derive dynamic equations of motions. Lagrangian is the difference between the kinetic and potential energy of a system.

$$\mathrm{L}(\dot{\theta},\,\theta)=\mathrm{T}(\dot{\theta},\theta)-\mathrm{V}(\theta) \tag{25}$$

Equations of motion can be derived from Lagrangian using Lagrange's equation

$$\tfrac{d}{dt}(\tfrac{\partial L}{\partial \theta})\;-\;\tfrac{\partial L}{\partial \theta}=\tau \tag{26}$$

Dynamic equations of motion were derived for front stage and back stage individually [17].

4.2.1 Front Stage Dynamics

In order to calculate dynamic equations of motion for front stage translational kinetic energy, rotational kinetic energy and potential energy of the system were calculated as

Kinetic Energy

$$\mathrm{T}_f=\mathrm{T}_{f_t}+T_{f_r} \tag{27}$$

where T_{f_t} is translational and T_{f_r} rotational kinetic energy.

$$\mathrm{T}_{f_t}=\dot{\theta_f^T}\begin{bmatrix}A_{11} & A_{12}\\ A_{21} & A_{22}\end{bmatrix}\dot{\theta_f} \tag{28}$$

$$\mathrm{T}_{f_r} = \dot{\theta_f^T} \begin{bmatrix} \frac{1}{2}(I_1 + I_3 + I_{d1}) & 0 \\ 0 & \frac{1}{2}(I_2 + I_4 + I_{d2} + I_g) \end{bmatrix} \dot{\theta_f} \tag{29}$$

where

$$\theta_f = \begin{bmatrix} \theta_1 \\ \theta_2 \end{bmatrix}$$

$$\mathrm{A}_{11} = m_1 l_{1c}^2 + m_3 l_{3c}^2 + m_4 l_1^2 + m_g l_1^2 + m_d d_1^2$$

$$A_{12} = (m_3 l_2 l_{3c} + m_4 l_1 l_{4c} + m_g l_1 l_4) cos(\theta_1 - \theta_2) + m_g l_1 l_g cos(\theta_1 - \theta_2 + \theta_g)$$

$$A_{54} = A_{45}$$

$$A_{21} = A_{12}$$

$$A_{22} = m_2 l_{2c}^2 + m_3 l_2^2 + m_4 l_{4c}^2 + m_g(l_4^2 + l_g^2 + \sqrt{2} l_4 l_g) + m_d d_2^2$$

(30)

In the equations m refers to mass, l refers to link length and d refers to distance between gimbal and last axis of links. θ_g is the angle between the gimbal and the link that it is assembled. θ_g was designed as 45°. For details see Figure 13.

Potential Energy

$$\mathrm{V}_f = [(m_1 l_{1c} + m_4 l_1 + m_3 l_{3c} + m_g l_1) sin(\theta_1) + (m_4 l_{4c} + m_2 l_{2c} + m_3 l_2 + m_g l_4) sin(\theta_2) + m_g l_g sin(\theta_2 - \theta_g) - m_d d_1 sin(\theta_d - \theta_1) + m_d d_2 sin(\theta_2 + \theta_d)\mathrm{g} \tag{31}$$

When we apply Lagrange's equation, dynamic equations of motion for front stage is found as

$$\begin{bmatrix} \tau_1 \\ \tau_2 \end{bmatrix} = \begin{bmatrix} \mathrm{M}_{11} & \mathrm{M}_{12} \\ \mathrm{M}_{21} & \mathrm{M}_{22} \end{bmatrix} \begin{bmatrix} \ddot{\theta_1} \\ \ddot{\theta_2} \end{bmatrix} + \begin{bmatrix} \mathrm{C}_1 \\ \mathrm{C}_2 \end{bmatrix} + \begin{bmatrix} \mathrm{G}_1 \\ \mathrm{G}_2 \end{bmatrix} \tag{32}$$

where

$$\mathrm{M}_{11} = A_{11} + I_1 + I_3 + I_{d1}$$

$$M_{12} = A_{12}$$

$$M_{21} = A_{21}$$

$$M_{22} = A_{22} + I_2 + I_4 + I_{d1} + I_g$$

$$C_1 = ((-m_3 l_2 l_{3c} - m_4 l_1 l_{4c} - m_g l_1 l_4) sin(\theta_1 - \theta_2) - m_g l_1 l_g sin(\theta_1 - \theta_2 + \theta_g))\dot{\theta}_1\dot{\theta}_2$$

$$C_2 = ((m_3 l_2 l_{3c} + m_4 l_1 l_{4c} + m_g l_1 l_4) sin(\theta_1 - \theta_2) + m_g l_1 l_g sin(\theta_1 - \theta_2 + \theta_g))\dot{\theta}_1\dot{\theta}_2$$

$$G_1 = -((m_1 l_{1c} + m_4 l_1 + m_3 l_{3c} + m_g l_1) cos(\theta_1) + m_d d_1 cos(\theta_d - \theta_1))g$$

$$G_2 = -((m_4 l_{4c} + m_2 l_{2c} + m_3 l_2 + m_g l_4) cos(\theta_2) + m_g l_g cos(\theta_2 - \theta_g) + m_d d_2 cos(\theta_2 + \theta_d))g$$

(33)

4.2.2 Back Stage Dynamics

In order to calculate dynamic equations of motion for back stage translational kinetic energy, rotational kinetic energy and potential energy of the system were calculated as

Kinetic Energy

$$\mathrm{T}_b = \mathrm{T}_{b_t} + T_{b_r} \tag{34}$$

$$\mathrm{T}_{b_t} = \dot{\theta_b^T} \begin{bmatrix} A_{33} & 0 & 0 \\ 0 & A_{44} & A_{45} \\ 0 & A_{54} & A_{55} \end{bmatrix} \dot{\theta}_b \tag{35}$$

$$\mathrm{T}_{b_r} = \dot{\theta_b^T} \begin{bmatrix} \frac{1}{2}(I_{base}) & 0 & 0 \\ 0 & \frac{1}{2}(I_1 + I_3 + I_{d1}) & 0 \\ 0 & 0 & \frac{1}{2}(I_2 + I_4 + I_{d2} + I_s) \end{bmatrix} \dot{\theta}_b \tag{36}$$

where

$$\theta_b = \begin{bmatrix} \theta_3 \\ \theta_4 \\ \theta_5 \end{bmatrix}$$

$$\mathrm{A}_{33} = m_1 l_{1c}^2 sin^2(\theta_4) + m_2 l_{2c}^2 sin^2(\theta_5) + m_d d_1^2 sin^2(\theta_4 - \theta_d) + m_d d_2^2 sin^2(\theta_5 + \theta_d) + m_3(l_2 sin(\theta_5) + l_{3c} sin(\theta_4))^2 + m_4(l_1 sin(\theta_4) + l_{4c} sin(\theta_5))^2 + m_s(l_1 sin(\theta_4) + l_4 sin(\theta_5) + l_s sin(\theta_5 - \theta_g))^2$$

$$A_{44} = m_1 l_{1c}^2 + m_3 l_{3c}^2 + m_4 l_1^2 + m_s l_1^2 + m_d d_1^2$$

$$A_{45} = (m_3 l_2 l_{3c} + m_4 l_1 l_{4c} + m_g l_1 l_4) cos(\theta_4 - \theta_5) + m_g l_1 l_g cos(\theta_4 - \theta_5 + \theta_g)$$

$$A_{54} = A_{45}$$

$$A_{55} = m_2 l_{2c}^2 + m_3 l_2^2 + m_4 l_{4c}^2 + m_g(l_4^2 + l_g^2 + \sqrt{2} l_4 l_g) + m_d d_2^2$$

(37)

In the equations m refers to mass, l refers to link length and d refers to distance between gimbal and last axis of links. For details see Figure 13.

Potential Energy

$$\mathrm{V}_b = ((m_1 l_{1c} + m_4 l_1 + m_3 l_{3c} + m_s l_1) sin(\theta_4) + (m_4 l_{4c} + m_2 l_{2c} + m_3 l_2 + m_s l_4) sin(\theta_5) + m_s l_s sin(\theta_5 - \theta_g) - m_d d_1 sin(\theta_d - \theta_4) + m_d d_2 sin(\theta_5 + \theta_d)) cos(\theta_3) g \tag{38}$$

When Lagrangian is found and Lagrange's equation is applied, dynamic equations of

motion for back stage is solved as

$$\begin{bmatrix} \tau_3 \\ \tau_4 \\ \tau_5 \end{bmatrix} = \begin{bmatrix} \mathrm{M}_{33} & 0 & 0 \\ 0 & \mathrm{M}_{44} & \mathrm{M}_{45} \\ 0 & \mathrm{M}_{54} & \mathrm{M}_{55} \end{bmatrix} \begin{bmatrix} \ddot{\theta}_3 \\ \ddot{\theta}_4 \\ \ddot{\theta}_5 \end{bmatrix} + \begin{bmatrix} \mathrm{C}_3 \\ \mathrm{C}_4 \\ \mathrm{C}_5 \end{bmatrix} + \begin{bmatrix} \mathrm{G}_3 \\ \mathrm{G}_4 \\ \mathrm{G}_5 \end{bmatrix} \tag{39}$$

where

$$\mathrm{M}_{33} = A_{33} + I_{base}$$

$$M_{44} = A_{44} + I_1 + I_3 + I_{d1}$$

$$M_{45} = A_{45}$$

$$M_{54} = A_{54}$$

$$M_{55} = A_{55} + I_2 + I_4 + I_{d1} + I_g$$

$$C_3 = 0$$

$$C_4 = (m_1 l_{1c}^2 sin(\theta_4)cos(\theta_4) + m_3 l_{3c} cos(\theta_4)(l_2 sin(\theta_5) + l_{3c} sin(\theta_4)) +$$
$$m_4 l_1 cos(\theta_4)(l_{4c} sin(\theta_5) + l_1 sin(\theta_4)) + m_d d_1^2 sin(\theta_4 - \theta_d)cos(\theta_4 - \theta_d) +$$
$$m_s l_1 cos(\theta_4)(l_4 sin(\theta_5) + l_1 sin(\theta_4) + l_s sin(\theta_5 - \theta_g)))\dot{\theta}_3^2 -$$
$$((m_3 l_2 l_{3c} + m_4 l_1 l_{4c} + m_s l_1 l_4)sin(\theta_4 - \theta_5) - m_s l_1 l_s sin(\theta_4 - \theta_5 + \theta_g))\dot{\theta}_4\dot{\theta}_5$$

$$C_5 = (m_2 l_{2c}^2 sin(\theta_5)cos(\theta_5) + m_4 l_{4c} cos(\theta_5)(l_{4c} sin(\theta_5) + l_1 sin(\theta_4)) +$$
$$m_3 l_2 cos(\theta_5)(l_2 sin(\theta_5) + l_{3c} sin(\theta_4)) + m_d d_2^2 sin(\theta_5 + \theta_d)cos(\theta_5 + \theta_d) +$$
$$m_s(l_4 cos(\theta_5) + l_s cos(\theta_5 - \theta_g))(l_4 sin(\theta_5) + l_1 sin(\theta_4) + l_s sin(\theta_5 - \theta_g)))\dot{\theta}_3^2 +$$
$$((m_3 l_2 l_{3c} + m_4 l_1 l_{4c} + m_s l_1 l_4)sin(\theta_4 - \theta_5) - m_s l_1 l_s sin(\theta_4 - \theta_5 + \theta_g))\dot{\theta}_4\dot{\theta}_5$$

$$G_3 = ((m_1 l_{1c} + m_4 l_1 + m_3 l_{3c} + m_s l_1)sin(\theta_4) + (m_4 l_{4c} + m_2 l_{2c} + m_3 l_2 + m_s l_4)sin(\theta_5) +$$
$$m_s l_s sin(\theta_5 - \theta_g) - m_d d_1 sin(\theta_d - \theta_4) + m_d d_2 sin(\theta_5 + \theta_d))sin(\theta_3)g$$

$$G_4 = -((m_1 l_{1c} + m_4 l_1 + m_3 l_{3c} + m_s l_1)cos(\theta_4) + m_d d_1 cos(\theta_d - \theta_4))cos(\theta_3)g$$

$$G_5 = -((m_4 l_{4c} + m_2 l_{2c} + m_3 l_2 + m_s l_4)cos(\theta_5) + m_s l_s cos(\theta_5 - \theta_g) + m_d d_2 cos(\theta_5 +$$
$$\theta_d))cos(\theta_3)g$$

(40)

Using the derived dynamic equation of motion, gravity compensation and controllers were implemented on the OBR. Details of gravity compensation and controllers will be given in Chapters V and VI.

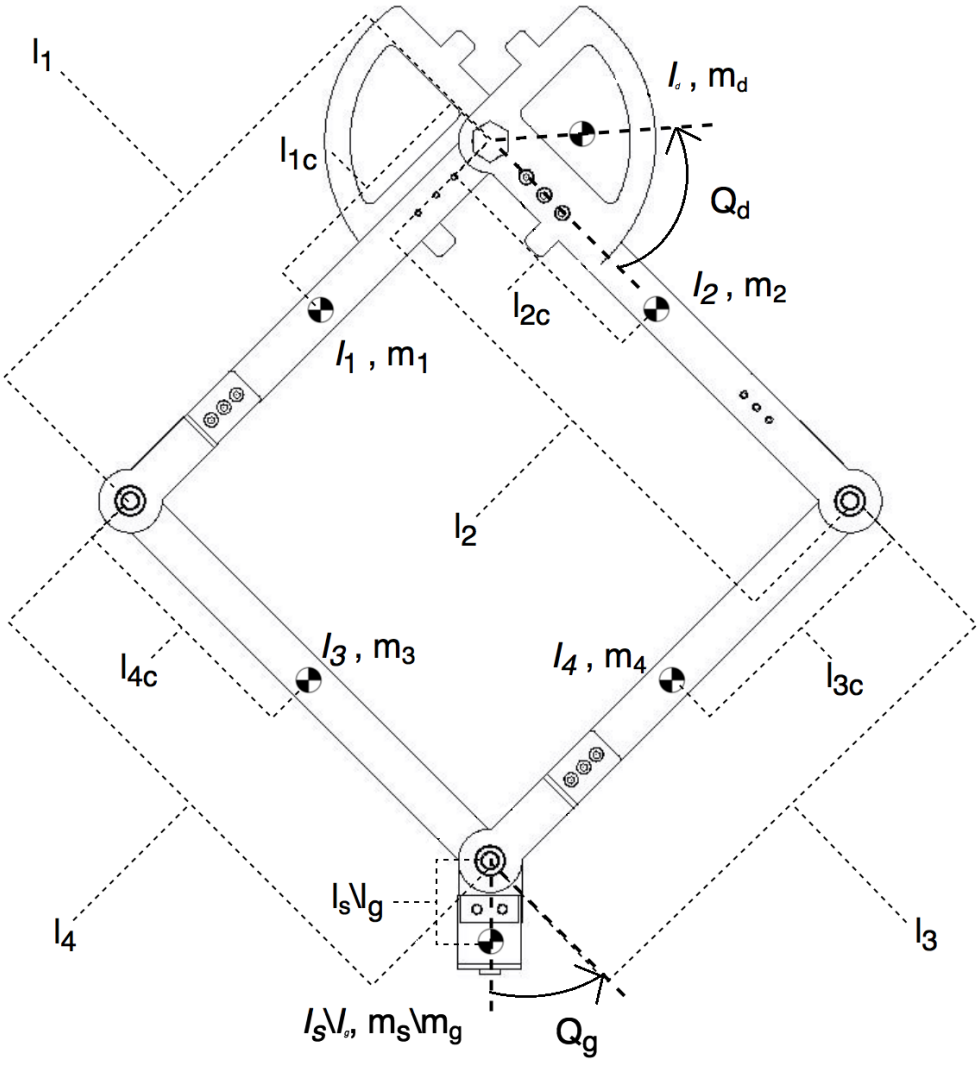

Figure 13: Center of gravity positions, link lengths of front stage and back stage for dynamic equations of motion

CHAPTER V

CALIBRATION AND MODELING

After designing and assembling OBR, to create an accurate controller, calibration and system modeling were performed on the robot. System identification were conducted on the robot to model dynamics of the system's motion. Calibration of the robot was carried out using OptiTrack motion capture system. Motion capture system consists of 6 OptiTrack S250e infrared motion capture cameras, Motive optical motion capture software and markers. Position of markers were detected using motion capture cameras according to a world coordinate system which is defined before calibration procedures. RMS error of motion capture system is $\pm$ 1 mm. All calibration procedure data was collected using Motive optical motion capture software at 10 Hz. In order to create a torque computed controller, gravity compensation and friction modeling was performed. All experiments were processed with MATLAB 2014b 64-bit on workstation with a processor Intel® Xeon® CPU E5-2620 @ 2.00 GHz 16 GB RAM. Quanser Q8 Data Acquisiton Board was used to get data from the robot and send data to the robot at 1kHz. ESCON 50/5 4Q Servocontrollers were used to drive the motors.

5.1 System Identification

In order to create an accurate controller for a system, dynamics of the system's motion should be known to designer; hence creating an accurate model of dynamic plant is a substantial step during controller design. In our system, one frequency at a time method was used [18]. If the system is described as

$$\mathrm{Y(z) = G(z)U(z) + H(z)W(z)} \tag{41}$$

where Y is plant output, U is plant input, W is unmeasured noise, G is plant transfer function and H is noise transfer function. If noise is assumed to be zero, plant transfer function can be calculated as

$$\begin{aligned} \mathrm{u(kT)} &= \mathrm{Asin(w_0}kT) \\ y(kT) &= Bsin(w_0kT + \phi_0) \\ \frac{B}{A} &= \left|G(e^{jw_0T})\right| \\ \phi_0 &= \angle \mathrm{G(e}^{jw_0T}) \end{aligned} \tag{42}$$

where A and B are amplitudes of the input and the output respectively. w_0 is the frequency and ϕ_0 is the phase between the input and the output. For different frequency values, magnitude and phase values of the system can be calculated using FFT of the system as

$$\frac{FFT(y)}{FFT(u)} = |G|\, e^{jw_0T} \tag{43}$$

For the experiments, 100 different frequency values which are logarithmically spaced were chosen between 1-100 Hz. A reference signal combining all the frequency values was created. The signal starts with 30 s of zero reference signal. It is followed by a sinusoidal signal at a specified frequency for again 30 s. This order is proceeded to combine signals of all frequency values into one reference signal. Reference signal was fed to the robot and response of the system was recorded from encoder data. The reason of using 30 s of data is to let the system to reach stable oscillation in steady-state region. Frequency response of the system was calculated using the reference signal. For every frequency value magnitude and phase of frequency response

was calculated using the above equations. Figure 14 shows the frequency response of the Axis1. A transfer function of the form s^4/s^6 was fit to the frequency response of the Axis1. The transfer function of the fit was used to create a pole placement controller for the system. However, the fit had unstable poles and the transfer function was uncontrollable. In order to have a controllable model, a reduced order transfer function with the form s^2/s^4 was fit to the frequency response of the system.

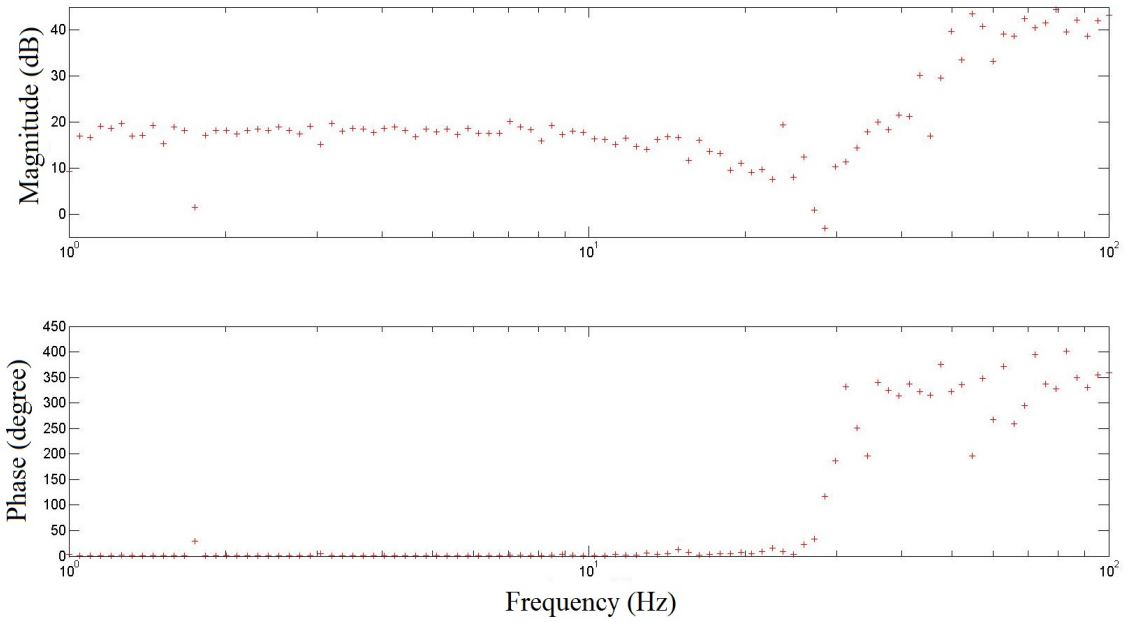

Figure 14: Frequency responce of Axis1 for frequencies between 1-100 Hz

Figure 15 shows the difference between s^4/s^6 and s^2/s^4 fits. s^4/s^6 order transfer function was trying to fit spikes in the experimental data. Therefore, s^2/s^4 fit was controllable and it was used to fit the transfer function to the frequency response of all axes. Figure 21 shows all fitting transfer functions to all axes. As seen from figure, the front stage axes (Axis1 and Axis2) show similar results with consistency. Behavior of the back stage axes (Axis4 and Axis5) also show same response. Reason of this is the rhombus structure of the design. As the results suggest, the front stage axes can keep their inertial behavior up to 30 Hz, however the back stage axes can only keep their inertial behavior up to 12 Hz. The reason for the difference is that

weight of the syringe mechanism is mostly carried by the back stage. The fitting models were analyzed to create pole placement controllers. Details of the controller will be given in the next chapter.

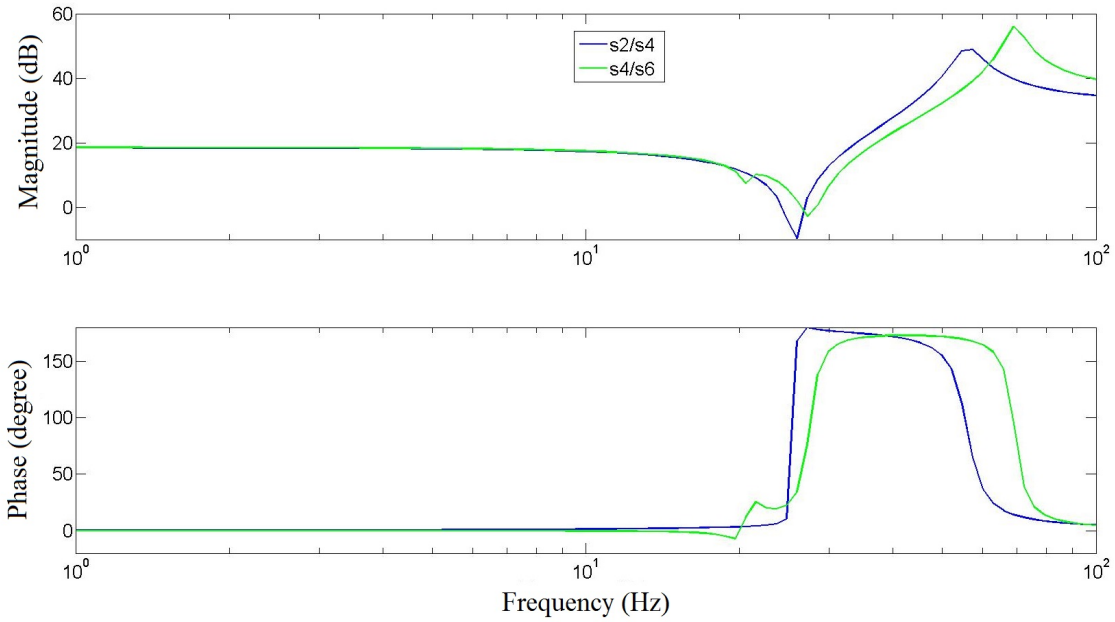

Figure 15: Comparison of s^2/s^4 to s^4/s^6 for frequency response of Axis1

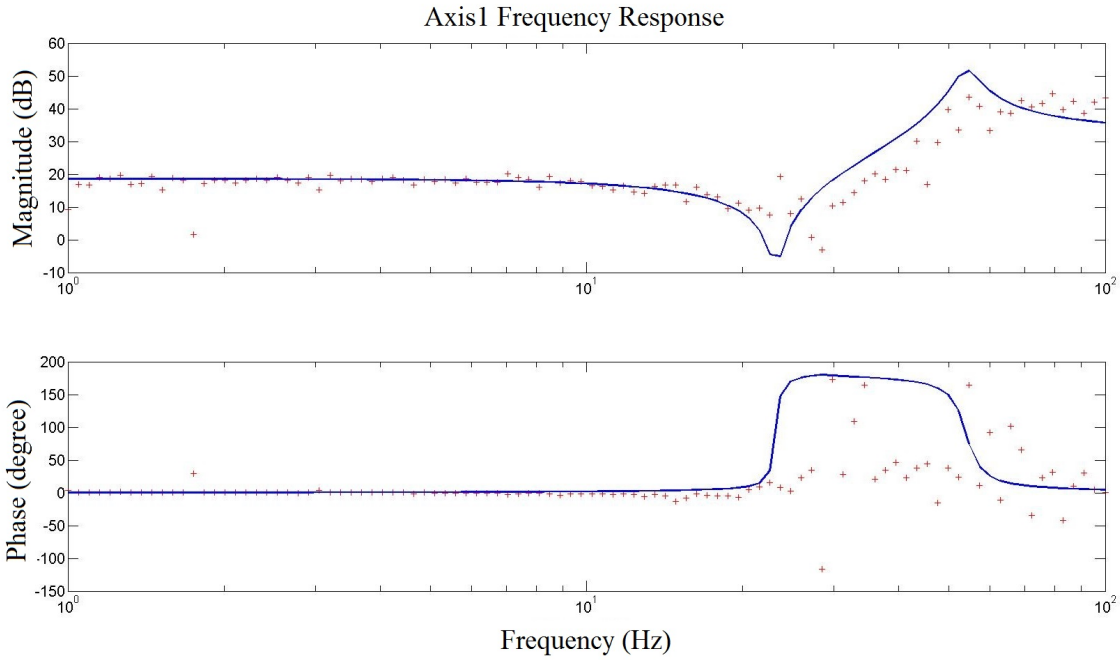

Figure 16: Frequency response fit for Axis1

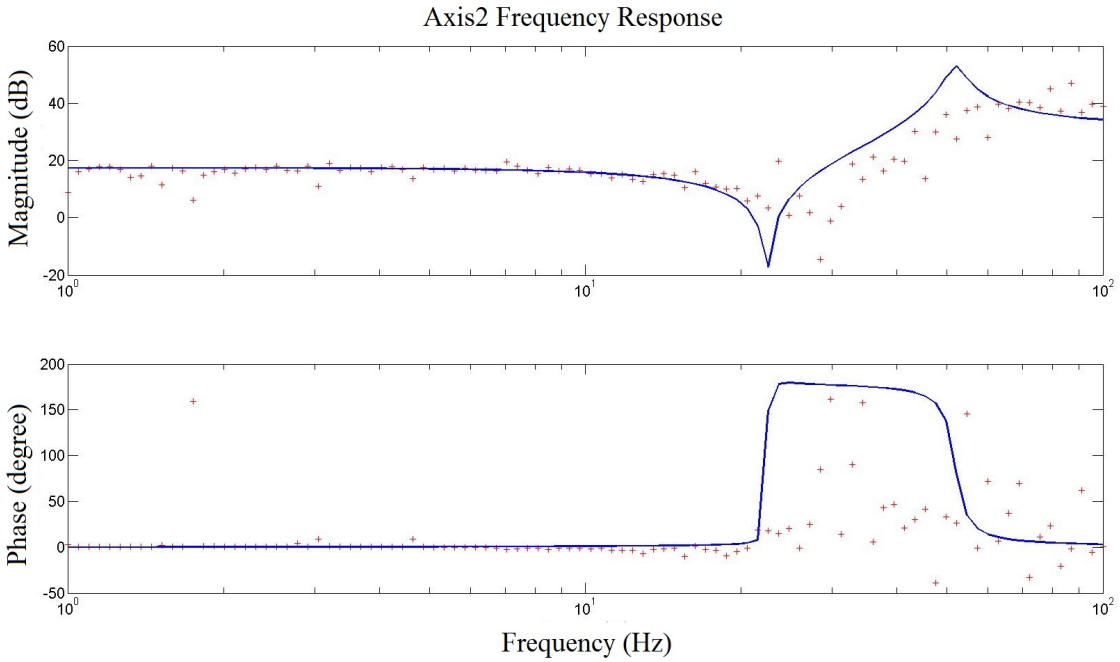

Figure 17: Frequency response fit for Axis2

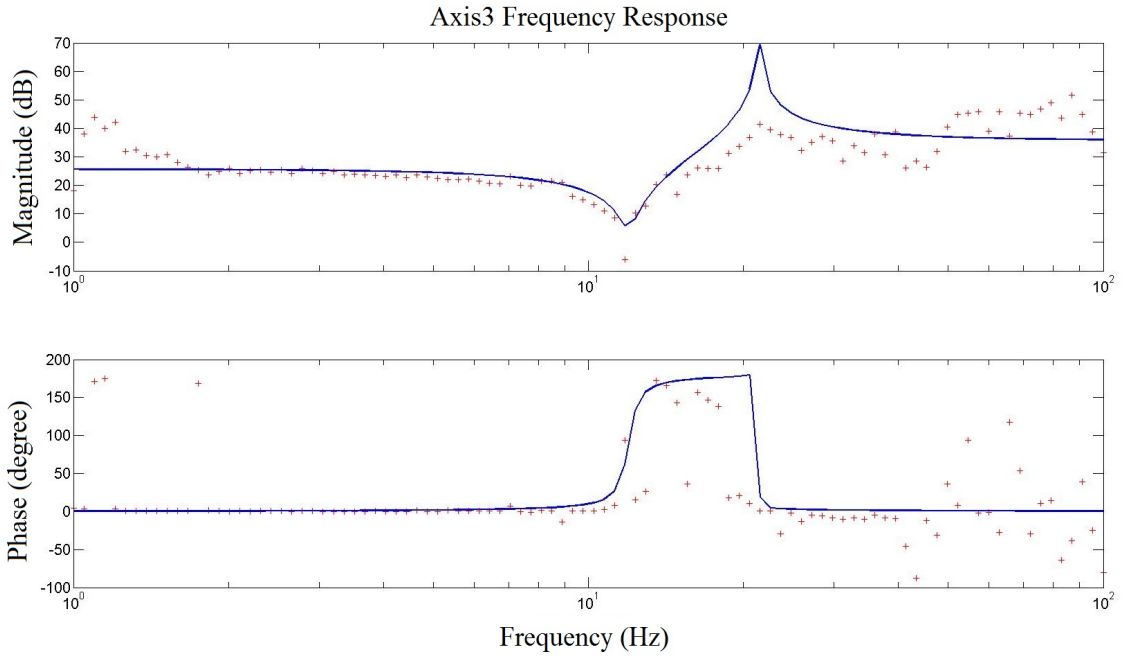

Figure 18: Frequency response fit for Axis3

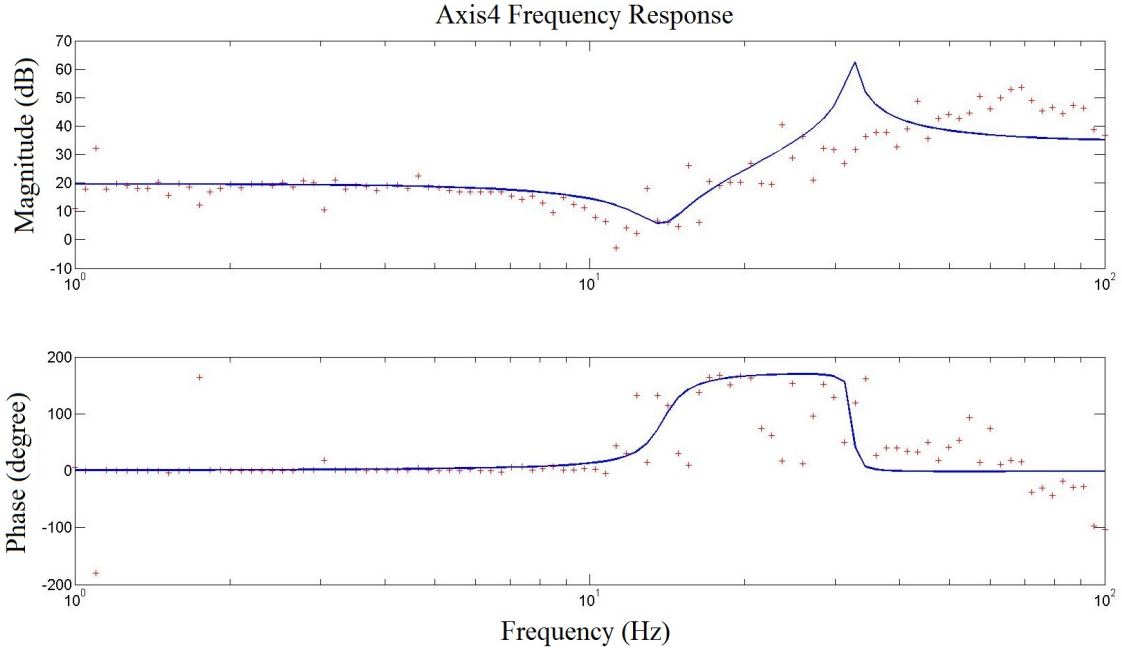

Figure 19: Frequency response fit for Axis4

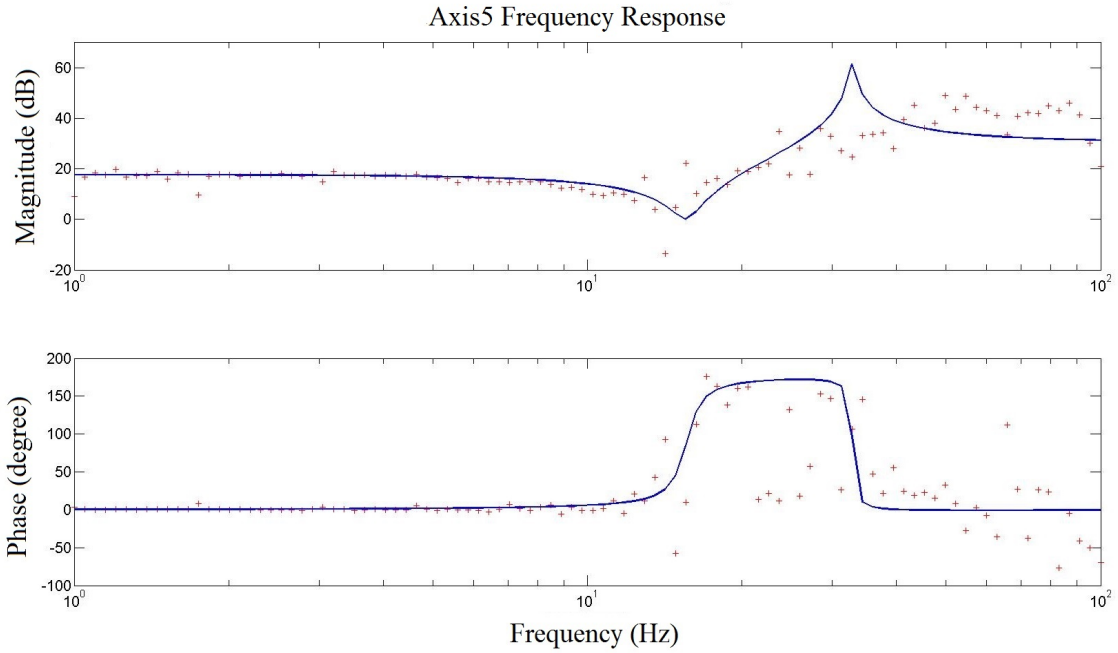

Figure 20: Frequency response fit Axis5

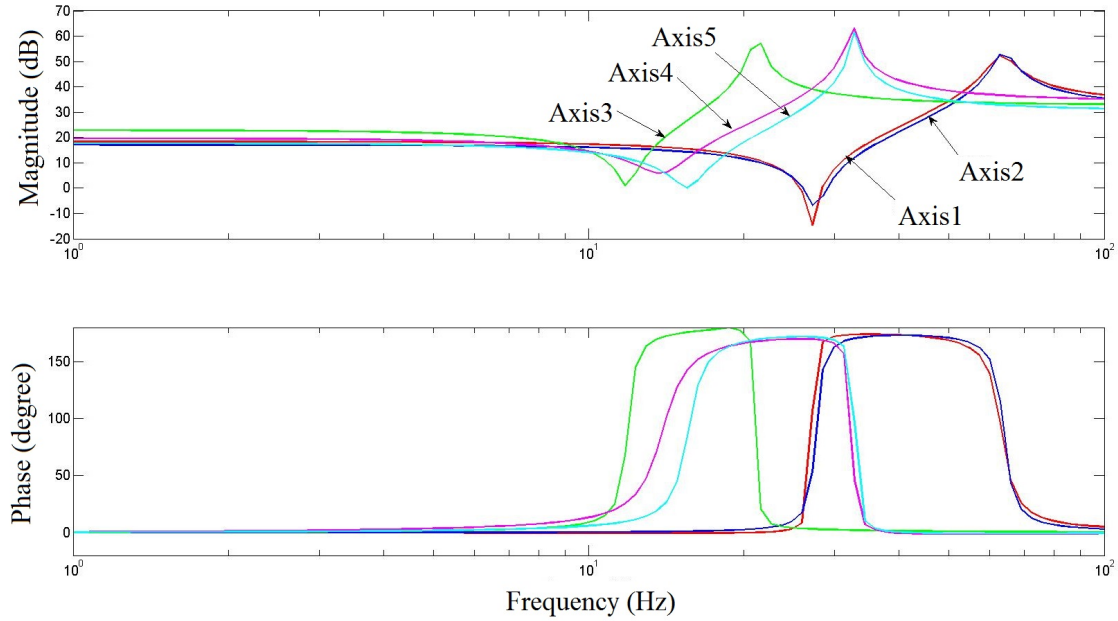

Figure 21: Frequency response fits for all axes of robot

5.2 Calibration

In order to increase the end effector position accuracy, calibration procedures was conducted on the robot. First calibration was performed on the misalignment between the front stage and back stage. On the design, syringe mechanism is assembled to the back stage, hence gimbal on back stage is longer than the gimbal on the front stage. To align the end effector positions of the front stage and the back stage on a line parallel to table surface, a misalignment between front stage base and back stage base was designed on the robot. Angular misalignment between two base could also occur during assembly process. To observe these misalignments on assembled robot, calibration was performed between front stage and back stage. As seen in Figure 22(a) two optical markers were placed on two bases and transformation matrix between two bases were obtained from OptiTrack system. Second calibration was conducted on tendon-driven mechanism. Despite the fact that no gear is used in the robot, due to usage of tendon-driven system, gear ratios were formed on each motor. In the calibration procedures, optical markers were attached to the links that are connected to different motors (Figure 22(b)). While the links were moving, encoder data from motors and angular position data from OptiTrack system were collected synchronically. A least square fit was processed on data to find gear ratios on each motor-link connection. Table 3 shows the gear ratios found from calibration and gear ratios expected from design. Lastly, due to design, robot has hardware limitations on its workspace. These limitations positions were calculated from Optitrack system data as angular positions and were included in kinematic calculations to increase the accuracy of needle tip position.

	Gear Ratios from Calibration	Gear Ratios from Design
Motor1	0.0874	0.0923
Motor2	0.0877	0.0923
Motor3	0.0752	0.0800
Motor4	0.0917	0.0923
Motor5	0.0878	0.0923

Table 3: Gear ratios calculated from calibration procedures and expected gear ratios from design specifications for each motor

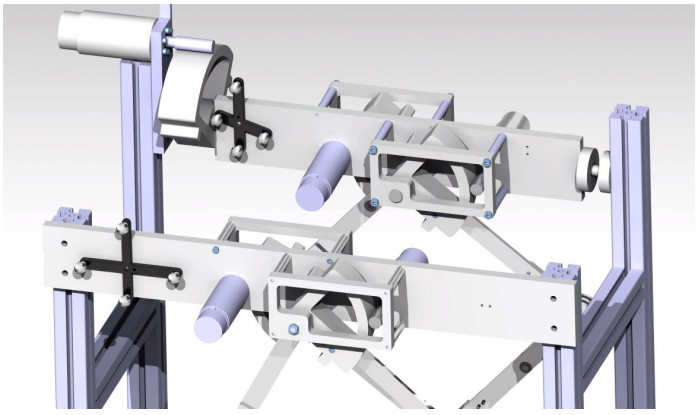

(a) Calibration between front stage and back stage

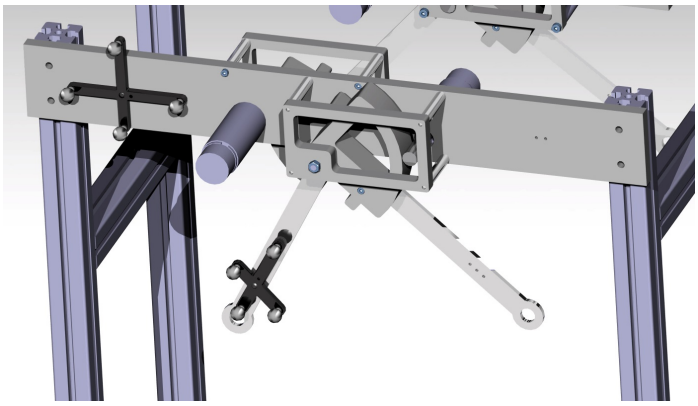

(b) Calibration of gear ratios

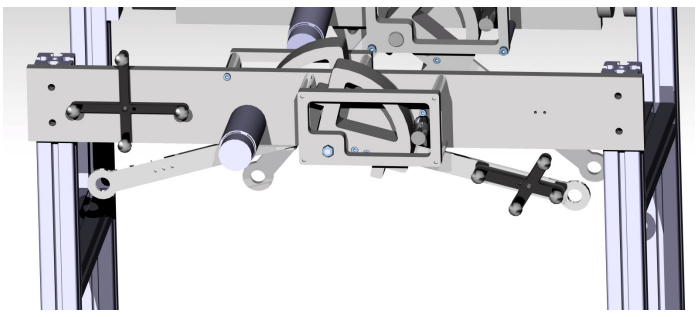

(c) Calibration of design limitations

Figure 22: Calibration procedure applied on Ozyegin Biopsy Robot

5.3 Gravity Compensation and Friction Modeling

Stiction and viscous friction forces are two elements affecting robot motion. Robot dynamics are insufficient to calculate stiction and viscous friction effects on each joint, hence a disturbance observer was created to observe the friction forces on the system [19]. On an accelerating system, there are four forces acting as disturbance; gravitational, frictional, external and inertial forces. As no external force is acting on the robot, disturbance observer would sense gravitational, inertial and frictional forces as disturbance. In order to observe only frictional forces as disturbance, dynamic equations of motion that were derived in Kinematics and Dynamics of Ozyegin Biopsy Robot chapter were used to compensate gravitational and inertial forces acting on each joint. Gravitational forces from robot dynamics were tested on the robot. Initial tests showed that except from Axis3, robot were able hold its position. Gravitational forces calculated for the Axis3 of the back stage are inadequate to hold the back stage in different positions while canceling the gravitational effects. In order to fix this issue, a simplified model was generated. Rhombus structure of the robot was simplified into one-bar mechanism which has a changing center of mass proportional to the change of orientation of rhombus structure. Figure 23 shows the simplified model. Therefore, whole back stage design was simplified into a one-bar mechanism and a gimbal connected to the end effector of one-bar mechanism. Gravitational force for Axis3 that is calculated from dynamic equations of motion was updated according to the simplified model. It is calculated as

$$G_3 = ((m_{bpar})(hsin(\theta_4 + \theta_A/2) + l_{bc}) + m_s(2hsin(\theta_4 + \theta_A/2) + l_s sin(\theta_5 - \theta_g)) + m_d d_1 sin(\theta_4 - \theta_d) + m_d d_2 sin(\theta_5 + \theta_d))sin(\theta_3)g \quad (44)$$

where

$$\theta_A = \theta_5 - \theta_4$$

$$h = l_1 cos(\theta_A/2) \tag{45}$$

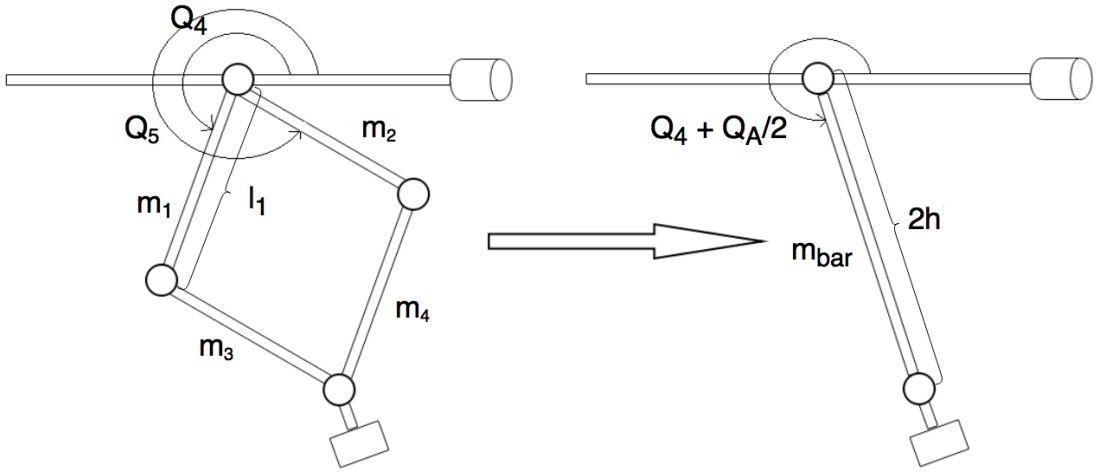

Figure 23: Simplified version of back stage for gravity compensation calculation

Experiments using simplified model showed that the Axis3 was able to hold the backstage in different positions while canceling the gravitational effects.

Next step after implementing gravity compensation was to create a disturbance observer to find frictional forces acting on each joint. Schematic of the disturbance observer can be seen in Figure 24. Disturbance observer output can be calculated from the schematic as

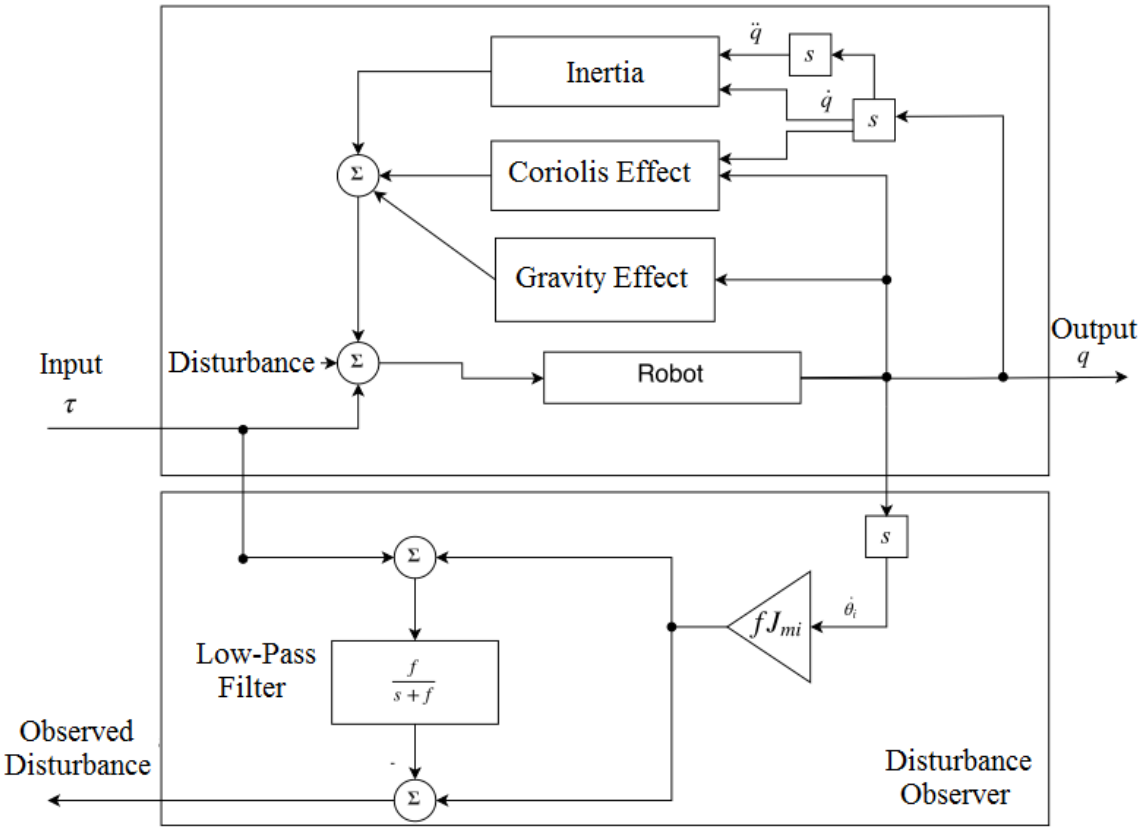

Figure 24: Disturbance observer schematic

$$\begin{aligned}
\widehat{T_{di}} &= fJ_{mi}s\theta_i - \tfrac{f}{s+f}(T_{ui} + fJ_{mi}s\theta_i) \\
\widehat{T_{di}} &= (\frac{s^2 J_{mi}\theta_i}{\frac{1}{f}s+1}) - (\frac{1}{\frac{1}{f}s+1})T_{ui} \\
\widehat{T_{di}} &\cong (J_{mi}\ddot{\theta}_i - T_{ui} = T_{di})
\end{aligned} \tag{46}$$

where T_{ui} is input torque, T_{di} is disturbance torque, $\widehat{T_{di}}$ is observed disturbance torque, J_{mi} is motor inertia and f is the frequency of low-pass filter. A ramp input was fed to each joint individually while gravity compensation was enabled on joints. It was thought that while the links are moving Coriolis effect would be sensed as disturbance, hence to cancel out the effect, using robot dynamics torque due to Coriolis effect was calculated and fed to the system with gravity terms. The frequency

for low-pass filter was chosen as 5 Hz. Different ramp inputs were fed to joints and disturbance observer data was recorded. As suggested inertial forces would be also observed as disturbance, hence inertial forces were calculated from dynamic equations of motion and were subtracted from recorded disturbance observer data. Figure 25-29 show the recorded disturbance observer data for all axes after subtracting inertial forces. It was observed that stiction and viscous friction is not showing a symmetry for positive and negative angular velocities as expected. Another observation was the non-increasing characteristics shown by axes. As the angular speed is increasing, friction shows stationary behavior. For all axes, friction models were created according to disturbance observer data. Friction models were also shown in Figure 25-29. The models were tested on each joint and tuned. Experiments showed that robot was moving as it is in a frictionless environment while both gravity and friction compensation were enabled.

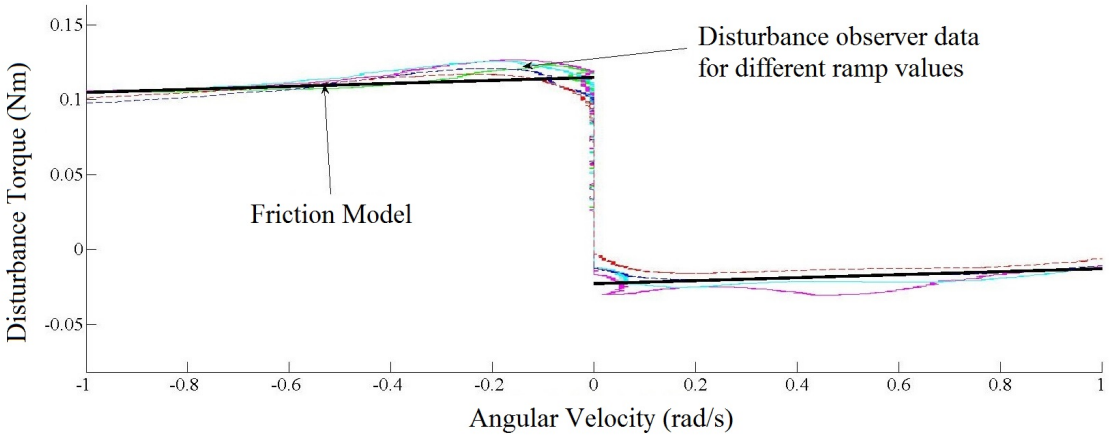

Figure 25: Stiction and viscous friction data using different ramp inputs and fitted friction model for Axis1

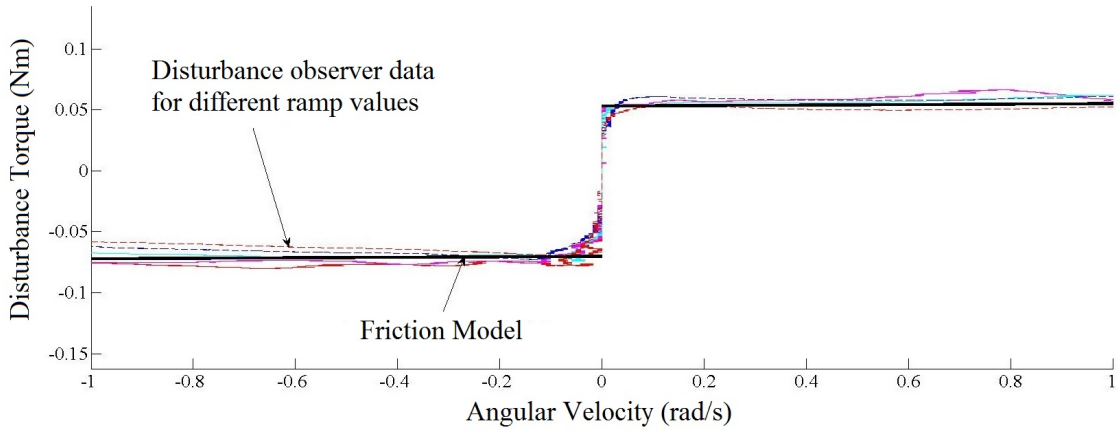

Figure 26: Stiction and viscous friction data using different ramp inputs and fitted friction model for Axis2

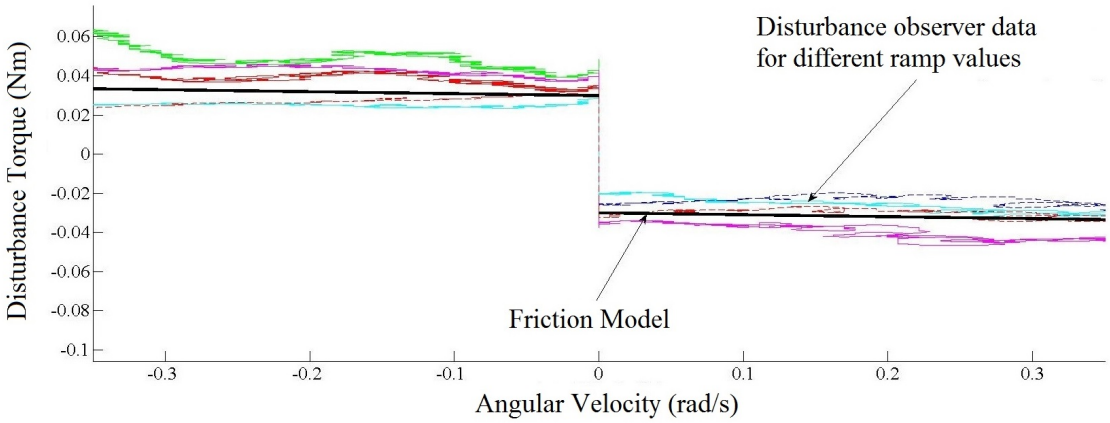

Figure 27: Stiction and viscous friction data using different ramp inputs and fitted friction model for Axis3

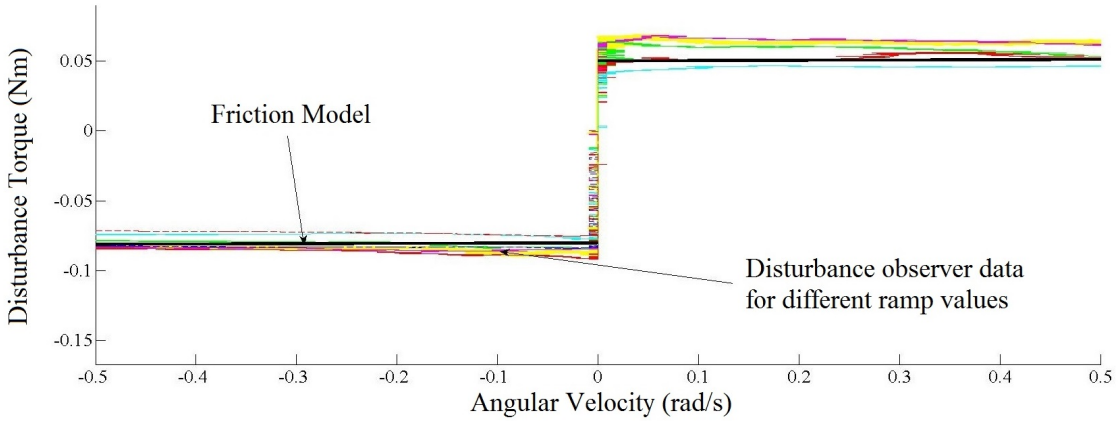

Figure 28: Stiction and viscous friction data using different ramp inputs and fitted friction model for Axis4

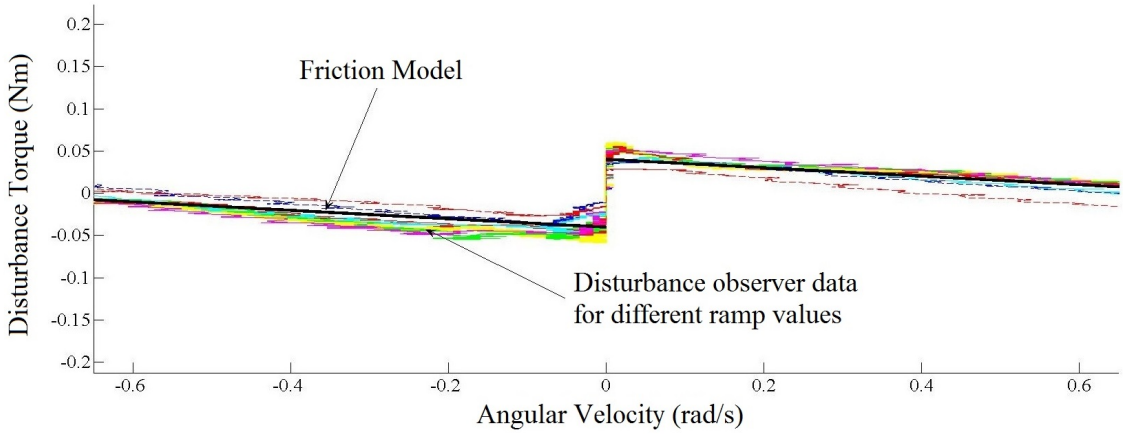

Figure 29: Stiction and viscous friction data using different ramp inputs and fitted friction model for Axis5

CHAPTER VI

CONTROL OF THE ROBOT

After specifying robot kinematics and dynamics, next step was to create an accurate controller to reach the desired needle tip position. Three different controllers were implemented to be tested on the robot, PID+Gravity controller, pole placement controller and torque computed controller. For PID+Gravity controller, system was controlled with a PID controller while the gravity compensation was enabled. Torque computed controller consists of a PD controller and compensated dynamic effects. Inertial, Coriolis and gravitational forces were calculated using the dynamic equations of motion and were fed to the robot as inputs. Friction models that were generated from disturbance observer were also introduced as input to compensate frictional forces. For pole placement, models that are derived during system identification were used. To verify the accuracy of controllers a path was created where the robot inserts the needle with a 30° insertion angle. Firstly, robot moves through the limit positions that are calculated in calibration procedures. Path for testing the controllers start from this position. From limit positions, robot moves to an orientation where it could insert the needle with a 30° insertion angle. After needle insertion orientation is reached, robot makes a translational motion along the needle axis. When the robot arrives the needle tip target position, it follows the translational motion trajectory in backward direction. Finally, robot moves toward its stationary position. Reference angles of the path were calculated using inverse kinematics of the robot and were fed to the robot to test the accuracy of controllers created. Encoder data from motors were recorded to calculate the accuracy of each controller.

6.1 PID+Gravity Controller

First controller tested on the robot was PID+Gravity Controller. A PID controller was created. Gains of the system were tuned using a sinusoidal signal. Controller was supported by gravity compensation. Gravitational forces were calculated from dynamic equations of motion and were fed to the robot as input. The reason of implementing a PID+Gravity controller instead of PID+Disturbance controller was that during gravity compensation and friction modeling experiments, it is seen that gravitational forces are higher than frictional forces. Therefore, implementing a PID+Disturbance controller would increase the effort of PID controller as the controller tries to compensate the gravitational effects. Table 4 shows the tuned gains of the controller. Results of the controller accuracy is given in Table 7.

Axis	K_p	K_i	K_d
Axis1	500	6	3
Axis2	700	6	5
Axis3	900	5	6
Axis4	300	5	3
Axis5	800	5	6

Table 4: Proportional, Integral and Derivative gains of PID+Gravity controller

6.2 Pole Placement Controller

Secondly, pole placement approach was used to create a controller. An observer was designed to predict the states of the system. The challenge of the controller design was to pick desired pole placement. The poles of fitting models were too close to unit circle. To design an accurate controller, both poles of observer and controller should be faster than poles of plant. In our system, it was impossible to choose faster poles for observer and controller. The selected poles for observer and controller are shown in Table 5. Results of the accuracy of controller is shown in Table 7.

Observer Poles	Controller Poles
0.99+0.1i	0.98+0.033i
0.99-0.1i	0.98-0.033i
0.9+0.43i	0.87+0.45i
0.9-0.43i	0.87-0.45i

Table 5: Desired observer and controller poles

6.3 Torque Computed Controller

Thirdly, a torque computed controller was chosen to be implemented on the robot. Figure 30 shows the schematic of the controller performed. While the robot is moving; inertial, Coriolis, gravitational and frictional forces act on the robot. The purpose of the controller is to cancel out these effect by feedforwarding the compensated inertial, Coriolis, gravitational and frictional torques into the control loop. Robot dynamics can be written as;

$$\tau_c + \tau_{ext} = M(q)\ddot{q} + C(q,\dot{q}) + G(q) + Fr(\dot{q}) \tag{47}$$

where τ_c is controller input, τ_{ext} is external force, M(q) is inertia matrix, C(q,$\dot{q}$) is Coriolis effect, G(q) is gravitational forces and Fr($\dot{q}$) is frictional forces acting on robot. Controller input can be chosen as

$$\tau_c = K_p q_e + K_d \dot{q_e} + M(q)\ddot{q_{ref}} + C(q,\dot{q}) + G(q) + Fr(\dot{q}) \tag{48}$$

where K_p and K_d are proportional and derivative gains. If no external force on the system is assumed, then error dynamics can be linearized as

$$K_p q_e + K_d \dot{q_e} + M(q)\ddot{q_e} = 0 \tag{49}$$

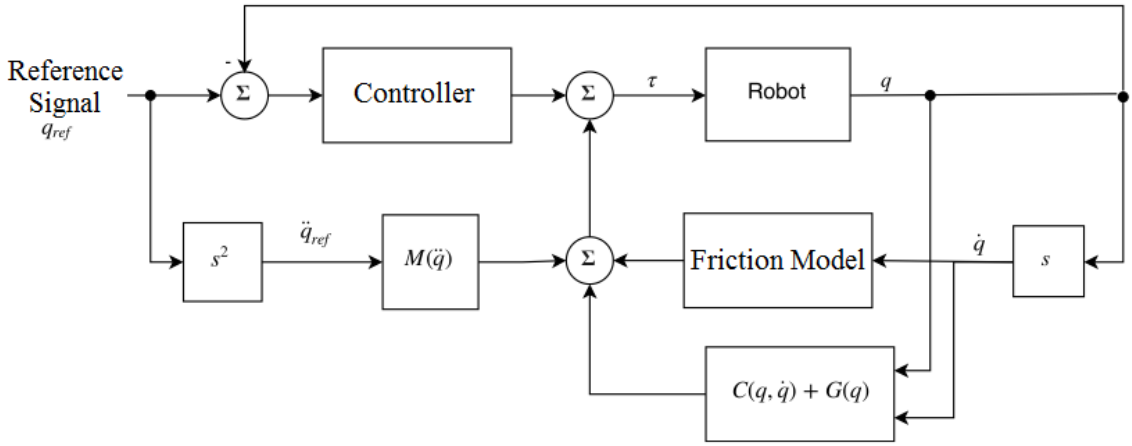

Figure 30: Torque compensated controller schematic

Figures 31-32-33 show the reference signal fed to Axis3, Axis4 and Axis5 respectively during needle insertion and needle pulling back. Output of controllers are also shown in the same figure. Table 7 shows the accuracy results of controllers for trajectory following of the path created. Results show that PID+Gravity controller has 1.56 mm, pole placement controller has 3.90 mm and torque computed controller has 0.678 mm RMS needle tip error. Even though pole placement controller shows sufficient results for controlling front stage axes, pole placement controller results for back stage axes were inaccurate. Reason of this inaccuracy is the location of poles of the fitting models. On the other hand, when PID-Gravity controller and torque computed controller results are compared, torque computed controller achieves more accurate results as expected. Reason of creating a torque computed controller was to feed forward inertial, Coriolis, gravitational and frictional effects as input to the system in order to decrease the controller effort. Error results and tuned controller gains for both controller support this reasoning. Torque computed controller ensures submilimeter needle tip accuracy, hence it is proved as a robust controller for the system.

Axis	K_p	K_d
Axis1	200	4
Axis2	200	4
Axis3	300	4
Axis4	200	4
Axis5	200	4

Table 6: Proportional and Derivative gains of Torque Computed controller

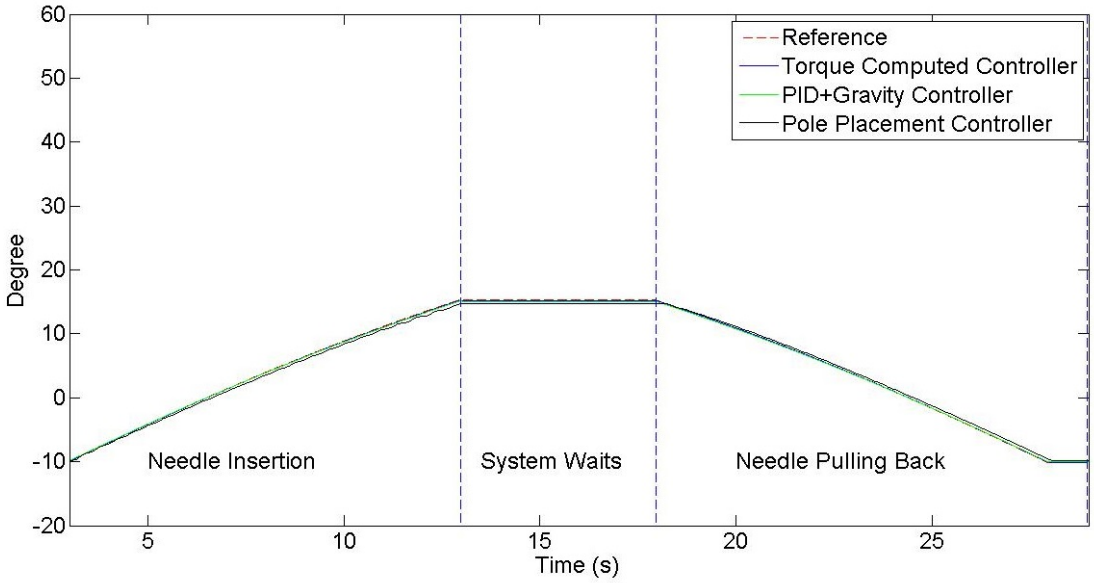

Figure 31: Reference signal fed to Axis3 during needle insertion and needle pulling back. Results of torque computed controller, PID+Gravity controller and pole placement controller are shown.

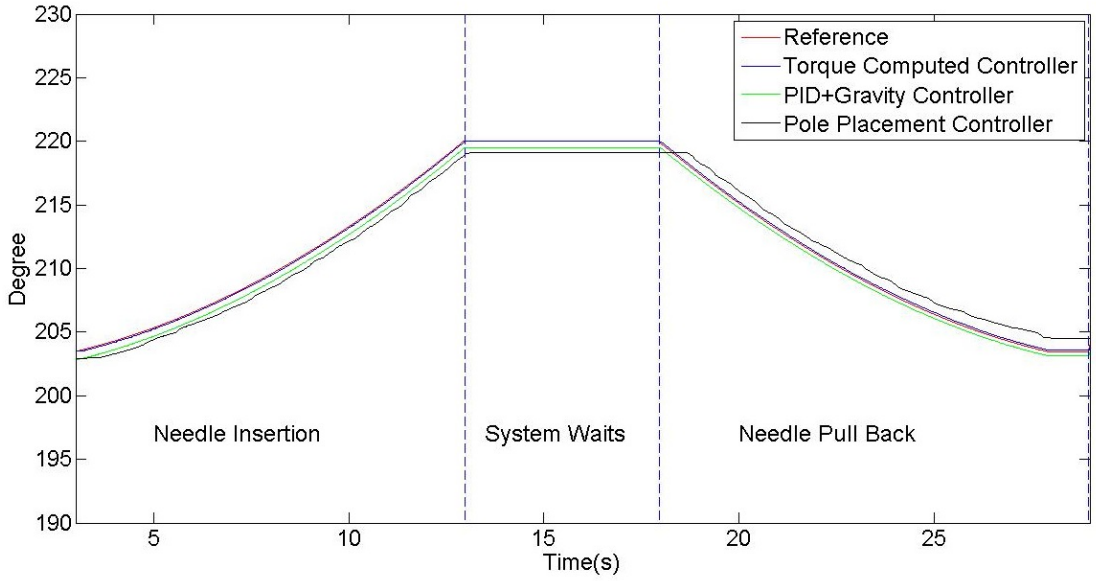

Figure 32: Reference signal fed to Axis4 during needle insertion and needle pulling back. Results of torque computed controller, PID+Gravity controller and pole placement controller are shown.

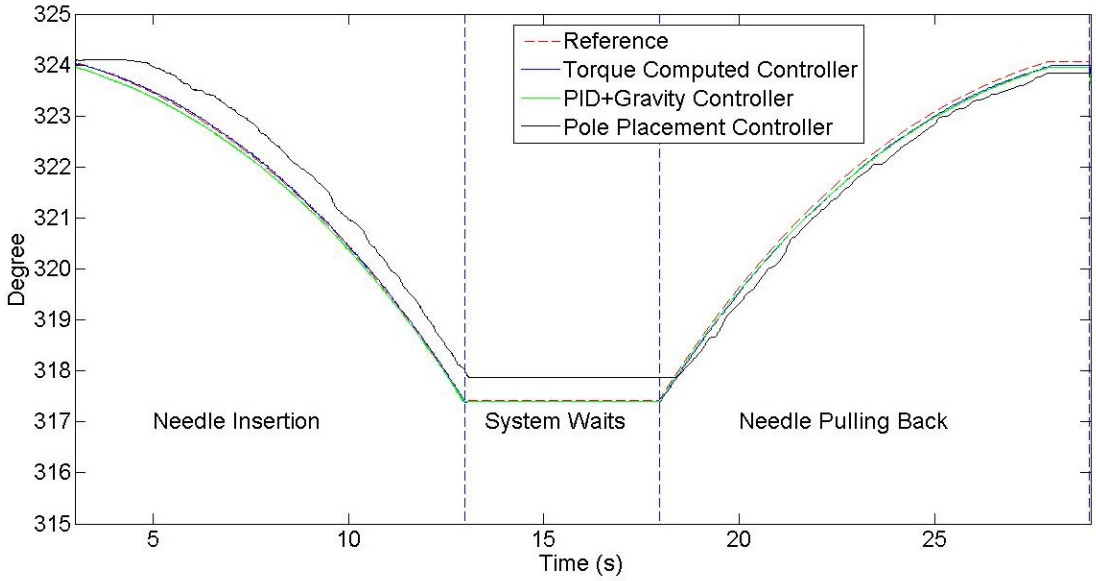

Figure 33: Reference signal fed to Axis5 during needle insertion and needle pulling back. Results of torque computed controller, PID+Gravity controller and pole placement controller are shown.

		Axis1	Axis2	Axis3	Axis4	Axis5	Front Stage End Effector	Back Stage End Effector	Needle Tip
		Degree					Millimeter		
PID + Gravity Controller	RMS	0.669	0.601	0.411	1.67	0.350	0.993	1.85	1.56
	Max	0.836	0.773	0.685	2.14	0.405	1.41	2.62	2.47
Pole Placement Controller	RMS	0.108	0.127	0.420	1.05	0.555	0.496	4.78	3.90
	Max	1.18	0.773	0.807	1.70	0.677	1.61	11.8	6.32
Torque Computed Controller	RMS	0.191	0.079	0.063	0.114	0.086	0.778	0.684	0.678
	Max	0.283	0.374	0.179	0.229	0.588	1.68	4.04	1.63

Table 7: Error results of controllers using the path created. Root mean square of errors and maximum error for each axis, end points of stages and needle tip are provided in the table. Errors for axises are given in degree. Errors for end points of stages and needle tip are given in millimeter.

CHAPTER VII

CONCLUSION

Reasoning behind this thesis was to design a robot that will conduct biopsies on human bodies. The robot will be the base of a 2D ultrasound image guided robotic system. The aim of the system is to perform biopsies fully autonomous. As explained before percutaneous needle operations needs precise positioning. Collected samples are important for the diagnostics, hence the samples must be collected from the exact place of the tumor or the anomaly for further analysis. The challenge of needle operations is to take enough samples with least number of trials to prevent damage to the healthy tissue. Robustness and accuracy of robotic systems would be a key factor to reduce the risk of false sample collection. In a single attempt, robot would get the correct sample from target position. Hospitalization time of patients would be reduced as the procedure will succeed in one single attempt. In overall, cost of the operation would be also decreased. Due to these reasoning, in this thesis design and modeling of a 5DOF parallel robot for biopsy procedures on human was presented.

To reach any desired position in 3D space in any desired orientation, a robot needs to have at least 6-DOF. As Ozyegin Biopsy Robot (OBR) would insert needle to the body, rotation around needle axis was redundant for the design of the robot. Therefore, OBR was designed to have 5-DOF. Robot divided into 3 parts; front stage, back stage and syringe mechanism. For front stage and back stage a rhombus mechanism that consists of 4 links was designed. Both stages have 2-DOF to control the end-effector of rhombus structure. An additional third DOF was added to back stage to provide the robot needle insertion capability, hence in total OBR has 5-DOF. Syringe mechanism that connects two stages was designed to collect sample

after needle insertion.

Aim of the robot is to conduct biopsy on abdominal region,hence workspace of the robot was decided to cover at least a cube of 50 cm. Necessary workspace analysis were performed in order to find minimum link lengths to reach 50 cm cube workspace goal. Calculations showed that link length of 200 mm would satisfy the goal. After finding appropriate link lengths, robot parts were designed. For tendon-driven mechanism, a disc to capstan ratio of 10.8 was used for Axis1, Axis2, Axis4 and Axis5. For Axis3 a bigger disc to capstan ratio was used, 12.5. Next step after designing to robot was to choose appropriate actuator. Torque analysis was conducted where the end effectors of stages were moved on a circle path. According to calculations, Maxon RE30 DC motor was chosen for Axis1 and Axis2, For Axis3, Axis4 and Axis5, a stronger motor was needed, Maxon RE40 DC motor.

In order to find accurate needle tip position, kinematic calculation was conducted on the robot design. Calculations were performed using Denavit-Hartenberg notations. Needle mounting offset was also considered in the kinematic calculation to increase the accuracy of needle tip. Dynamic equations of motion were derived in order to create accurate controllers for the system. Calculations were performed using Lagrange's equation. System identification were also carried out to find system dynamics in order to create accurate controllers. Calibration procedures are conducted on robot to increase the accuracy of the system. First, a transformation matrix between front stage and back stage were calculated in order to find the misalignment between two stages. Secondly, gear ratios on each motor were calculated. Even no gear is used on the system, due to tendon-driven mechanism gear ratios were formed on each motor. Thirdly, mechanical limitation were measured and were used in kinematic calculation of end-effector position. After calibration of the robot, gravity compensation and friction modeling were performed on the robot. Gravity compensation was implemented using robot dynamics. For Axis3, a simplified model

of back stage was created to fulfill gravity compensation. A disturbance observer was created to find the stiction and viscous frictional forces acting on joints. According to experimental data, friction models for each joint was created.

Three different controllers were implemented onto OBR; PID+Gravity contoller, pole placement controller and torque computed controller. For PID+Gravity controller and torque computed controller, dynamic equations of motion were used. For pole placement controller, models from system identification were used. Controllers were tested on a path where the robot inserts needle with 30° insertion angle. Results showed that pole placement controller was a weak controller for the system. Controller reached a RMS needle tip accuracy of 3.90 mm. The reason was that pole locations of fitting models were close to unit circle. In order to create an accurate, robust controller with pole placement method, controller poles should be faster than system poles. For the fitting models of system identification procedures, choosing faster poles was not feasible, hence pole placement controller showed inaccurate results. When PID+Gravity controller and torque computed controller were compared, torque computed controller showed more accurate results. PID+Gravity controller reached an RMS needle tip accuracy of 1.56 mm. On the other hand torque computed controller reached an RMS needle tip accuracy of 0.678 mm. The reason of implementing a torque computed controller was to feed inertial, Coriolis, gravitational and frictional forces as an input to the system in order to decrease the controller effort against a classical PID controller. According to results torque computed controller reached a submilimeter needle tip accuracy and controller is verified as a robust controller for the system.

As torque computed controller was verified as a robust controller for the system, next step for the development of the OBR is to implement a force feedback architecture. During the insertion of the needle, force is applied to the needle tip from the body. Applied force causes the needle to bend and changes the needle tip position.

In order to calculate accurate needle tip position, bending of the needle should be included in the kinematic calculations. To find the bending of the needle, force on the needle tip should be known to the controller. Syringe mechanism could be modified to have a force sensor in order to calculate the force applied to the needle tip from the body. Using the force feedback data, the needle could be modeled as a simple beam and deflection of the needle tip could be found accurately. Calculating deflection is also a key step for needle tip estimation from 2D ultrasound images. As the needle is seen as straight in the ultrasound images, including deflection on the needle tip would increase accuracy of needle tip estimation. Overall, needle tip deflection due to force applied from the body to the needle could be calculated and included to kinematic calculations in order to increase target reach accuracy.

Bibliography

[1] O. Bebek, M. J. Hwang, and M. C. Cavusoglu, "Design of a parallel robot for needle-based interventions on small animals," *Mechatronics, IEEE/ASME Transactions on*, vol. 18, no. 1, pp. 62–73, 2013.

[2] Y. Moon and J. Choi, "A compliant parallel mechanism for needle intervention," in *Engineering in Medicine and Biology Society (EMBC), 2013 35th Annual International Conference of the IEEE*, pp. 4875–4878, IEEE, 2013.

[3] Y. Zhou, K. Thiruvalluvan, L. Krzeminski, W. Moore, Z. Xu, and Z. Liang, "An experimental system for robotic needle biopsy of lung nodules with respiratory motion," in *Mechatronics and Automation (ICMA), 2011 International Conference on*, pp. 823–830, Aug 2011.

[4] A. Majewicz, S. P. Marra, M. G. van Vledder, M. Lin, M. A. Choti, D. Y. Song, and A. M. Okamura, "Behavior of tip-steerable needles in ex vivo and in vivo tissue," *Biomedical Engineering, IEEE Transactions on*, vol. 59, no. 10, pp. 2705–2715, 2012.

[5] N. Tanaiutchawoot, C. Wiratkapan, B. Treepong, and J. Suthakorn, "On the design of a biopsy needle-holding robot for a novel breast biopsy robotic navigation system," in *Cyber Technology in Automation, Control, and Intelligent Systems (CYBER), 2014 IEEE 4th Annual International Conference on*, pp. 480–484, IEEE, 2014.

[6] B. Yang, U.-X. Tan, A. McMillan, R. Gullapalli, and J. P. Desai, "Design and implementation of a pneumatically-actuated robot for breast biopsy under continuous mri," in *Robotics and Automation (ICRA), 2011 IEEE International Conference on*, pp. 674–679, IEEE, 2011.

[7] T. Nelson, A. Tran, H. Farourfar, and J. Nebekert, "Ultrasound image-guided robotic breast biopsy," in *Ultrasonics Symposium (IUS), 2010 IEEE*, pp. 2352–2355, Oct 2010.

[8] V. Mallapragada, N. Sarkar, and T. Podder, "Toward a robot-assisted breast intervention system," *Mechatronics, IEEE/ASME Transactions on*, vol. 16, pp. 1011–1020, Dec 2011.

[9] H. Zaidi, Y. Chao, Z. Lei, and Y. Wang, "Design and optimization analysis of open-mri compatibile robot for neurosurgery," in *Bioinformatics and Biomedical Engineering, 2008. ICBBE 2008. The 2nd International Conference on*, pp. 1773–1776, IEEE, 2008.

[10] C. Raoufi, A. Goldenberg, and W. Kucharczyk, "A new hydraulically/pneumatically actuated mr-compatible robot for mri-guided neurosurgery,"

in *Bioinformatics and Biomedical Engineering, 2008. ICBBE 2008. The 2nd International Conference on*, pp. 2232–2235, May 2008.

[11] A. Melzer, B. Gutmann, T. Remmele, R. Wolf, A. Lukoscheck, M. Bock, H. Bardenheuer, and H. Fischer, "Innomotion for percutaneous image-guided interventions," *Engineering in Medicine and Biology Magazine, IEEE*, vol. 27, pp. 66–73, May 2008.

[12] J. Chung, H.-J. Cha, B.-J. Yi, and W. K. Kim, "Implementation of a 4-dof parallel mechanism as a needle insertion device," in *Robotics and Automation (ICRA), 2010 IEEE International Conference on*, pp. 662–668, IEEE, 2010.

[13] L. Goffin, G. Bour, F. Martel, S. Nicolau, J. Gangloff, J.-M. Egly, and B. Bayle, "Design and in vivo evaluation of a robotized needle insertion system for small animals," *Biomedical Engineering, IEEE Transactions on*, vol. 60, no. 8, pp. 2193–2204, 2013.

[14] Y. Huang, T. Wu, M. Lin, C. Yang, W. Guo, Z. Wang, C. Chen, and J. Lee, "An automated robot arm system for small animal tissue biopsy under dual-image modality," *Nuclear Instruments and Methods in Physics Research Section A: Accelerators, Spectrometers, Detectors and Associated Equipment*, vol. 569, no. 2, pp. 230–234, 2006.

[15] A. Waspe, H. Cakiroglu, J. Lacefield, and A. Fenster, "Design and validation of a robotic needle positioning system for small animal imaging applications," in *Engineering in Medicine and Biology Society, 2006. EMBS '06. 28th Annual International Conference of the IEEE*, pp. 412–415, Aug 2006.

[16] Y. Moon and J. Choi, "A planar compliant parallel robotic mechanism for robotic needle intervention," in *Control, Automation and Systems (ICCAS), 2013 13th International Conference on*, pp. 92–95, IEEE, 2013.

[17] M. Hwang, O. Bebek, and C. Cavusoglu, "Kinematics and dynamics of small animal biopsy robot (sabir)," tech. rep., 2011.

[18] G. F. Franklin, J. D. Powell, and M. L. Workman, *Digital control of dynamic systems*, vol. 3. Addison-wesley Menlo Park, 1998.

[19] B. Ugurlu, M. Nishimura, K. Hyodo, M. Kawanishi, and T. Narikiyo, "Proof of concept for robot-aided upper limb rehabilitation using disturbance observers," *Human-Machine Systems, IEEE Transactions on*, vol. 45, pp. 110–118, Feb 2015.

[20] D. Stoianovici, L. L. Whitcomb, J. H. Anderson, R. H. Taylor, and L. R. Kavoussi, "A modular surgical robotic system for image guided percutaneous procedures," in *Medical Image Computing and Computer-Assisted Intervention - MICCAI'98, First International Conference, Cambridge, MA, USA, October 11-13, 1998, Proceedings*, pp. 404–410, 1998.

VITA

Sabri Orçun Orhan received his B.S. degree in Mechatronics from Sabancı University in 2011. He pursued M.S. in Mechanical Engineering at Ozyegin University and worked as Teaching/Research Assistant between 2012-2015. His research interest includes Medical Robotics Design and Control.